Click Here for Full Article

Protracted construction of gabbroic crust at a slow spreading ridge: Constraints from ^{206}Pb/^{238}U zircon ages from Atlantis Massif and IODP Hole U1309D (30°N, MAR)

Craig B. Grimes, Barbara E. John, and Michael J. Cheadle
Department of Geology and Geophysics, University of Wyoming, 1000 East University Avenue, Laramie, Wyoming 82071, USA (cgrimes@uwyo.edu)

Joseph L. Wooden
U.S. Geological Survey–Stanford Ion Microprobe Laboratory, Green Earth Sciences Building, 367 Panama Street, Room 89, Stanford, California 94305, USA

[1] Sensitive high-resolution ion microprobe (SHRIMP) U-Pb zircon ages of 24 samples from oceanic crust recovered in Integrated Ocean Drilling Program (IODP) Hole U1309D and from the surface of Atlantis Massif, Mid-Atlantic Ridge (MAR) (30°N) document a protracted history of accretion in the footwall to an oceanic detachment fault. Ages for 18 samples of evolved Fe-Ti oxide gabbro and felsic dikes collected 40–1415 m below seafloor in U1309D yield a weighted mean of 1.20 ± 0.03 Ma (mean square of weighted deviates = 7.1). However, the ages range from 1.08 ± 0.07 Ma and 1.28 ± 0.05 Ma indicating crustal construction occurred over a minimum of 100–200 ka. The zircon ages, along with petrologic observations, indicate at least 2 major periods of intrusive activity with age peaks separated by 70 ka. The oldest ages are observed below 600 mbsf, an observation inconsistent with models requiring constant depth melt intrusion beneath a detachment fault. The data are most consistent with a "multiple sill" model whereby sills intrude at random depths below the ridge axis over a length scale greater than 1.4 km. Zircon ages from broadly spaced samples collected along the southern ridge of Atlantis Massif yield a detachment fault slip rate of 28.7 ± 6.7 mm/a and imply significant asymmetric plate spreading (up to 100% on the North American plate) for at least 200 ka during core complex formation.

1. Introduction

[2] One of the major limitations to understanding the magmatic growth of oceanic crust is the difficulty obtaining precise absolute age relationships in mafic and ultramafic rocks [*Meurer and Gee*, 2002]. Over the past 10–15 years, however, improved seafloor sampling has led to the recovery of numerous sections of gabbroic crust that include evolved rock types that host accessory minerals amenable to isotopic age studies, particularly zircon [e.g., *Gillis et al.*, 1993; *Cannat and Casey*, 1995; *Dick et al.*, 2000; *Schroeder and John*, 2004; *Kelemen et al.*, 2004; *Blackman et al.*, 2006]. Isotopic ages from zircon in ocean crust have thus far been used to gain insight into crystallization ages of gabbroic massifs, as well as cooling rates of ocean lithosphere, and plate spreading rates in conjunction with paleomagnetic studies to further our understanding of crustal accretion along the southwest Indian Ridge (SWIR) [*John et al.*, 2004; *Schwartz et al.*, 2005; *Baines*, 2006] and Mid-Atlantic Ridge (MAR) [*Grimes et al.*, 2007a].

[3] In the present contribution, we use $^{206}Pb/^{238}U$ isotopic ages of zircon from Atlantis Massif at 30°N on the slow spreading MAR to investigate the absolute timing, duration and patterns of magma emplacement that led to the development of a 1.4 km gabbroic crustal section sampled during Integrated Ocean Drilling Program (IODP) drilling of the Atlantis Massif oceanic core complex. Incorporating additional samples collected by manned submersible and dredge across the southern ridge of Atlantis Massif, we are able to evaluate local spreading rates during formation of the core complex, and speculate on the depths of gabbro emplacement.

2. Tectonic Setting of the Mid-Atlantic Ridge, 30°N and Atlantis Massif

2.1. Atlantis Massif

[4] Atlantis Massif is located near 30°N at the intersection of the slow spreading Mid-Atlantic Ridge (MAR) (full-spreading rate ~23.6 mm/a, Nuvel-1 model) and the Atlantis Transform Fault (Figure 1). The corrugated central portion of the domal massif is inferred to represent an oceanic core complex exposed via long-lived detachment faulting [*Cann et al.*, 1997; *Blackman et al.*, 1998, 2002], possibly analogous to core complexes observed in continental settings [*John*, 1987; *Davis and Lister*, 1988]. The footwall at Atlantis Massif is composed of lower crust and upper mantle rocks, denuded by the detachment fault that is exposed over an 8–10 km wide, 15 km long area that forms the elongate, doubly plunging domal seafloor morphology. The seafloor dips ~5° away from the ridge axis (west) on the western side of the dome, and rolls over to dip gently (~12°) toward the ridge-axis (east) before disappearing beneath an eastern block composed of basalt (Figure 1). It is suggested that the eastern block represents the hanging wall to the detachment fault [*Blackman et al.*, 2006]. Alternatively, the block could represent a sequence of gently tilted lavas erupted directly onto the detachment surface, in the rift valley, and subsequently uplifted by a younger normal fault [*Blackman et al.*, 2002].

[5] The southern ridge adjacent to the Atlantis Transform rises to approximately 700 m below sea level, nearly 1 km above the central dome. This portion of Atlantis Massif has been mapped extensively by submersible, and samples recovered comprise 70% peridotite, with the remaining 30% dominated by gabbro as small, centimeter- to meter-scale intrusive bodies [*Blackman et al.*, 2002; *Karson et al.*, 2006]. Brittle fault rocks are concentrated structurally within ~90 m of the upper surface, consistent with the view that this surface represents a detachment fault [*Schroeder and John*, 2004; *Boschi et al.*, 2006], and that while active this fault acted as the plate boundary [*Schroeder and John*, 2004; *Buck et al.*, 2005].

2.2. IODP Hole U1309D

[6] In the winter of 2004–2005, IODP Expeditions 304 and 305 drilled holes in both the footwall and proposed hanging wall blocks of Atlantis Massif. The deepest hole, U1309D, was spud ~14 km west of the axial valley on the central dome of Atlantis Massif, where the seafloor coincides with the detachment fault surface (Figure 1). Sea surface magnetic anomalies provide an overall temporal framework for the development of Atlantis Massif, but alone do not allow a precise age determination for Site U1309 [*Pariso et al.*, 1996; *Blackman et al.*, 2006]. They indicate broadly symmetric time-integrated half-spreading rates of 11–12 mm/a over Atlantis Massif during the past ~2 Ma [*Zervas et al.*, 1995; *Pariso et al.*, 1996]. Near-bottom magnetic measurements indicate that U1309D is located several kilometers east of a small positive magnetic anomaly that may represent Anomaly
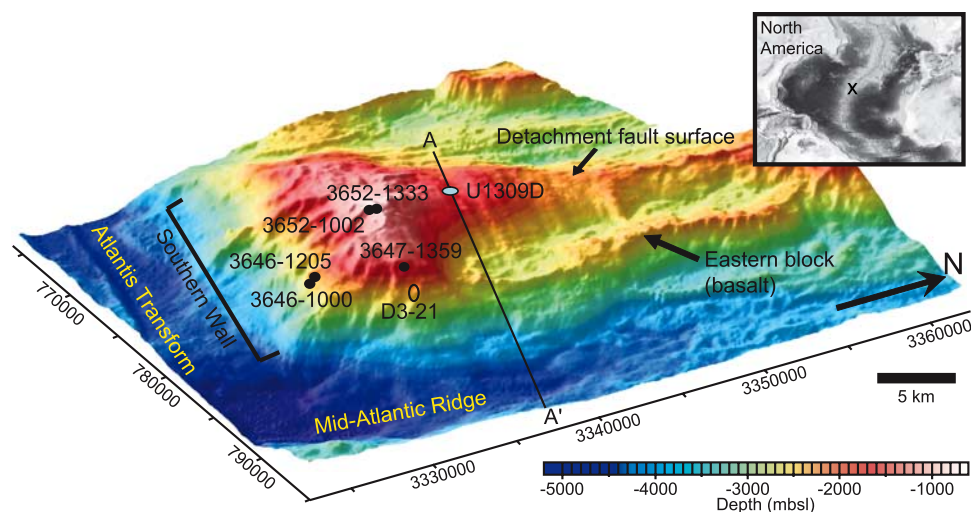
Figure 1. Oblique view of Atlantis Massif (looking WNW). IODP Hole U1309D is indicated on the corrugated detachment fault surface, and the locations of additional submersible dive and dredge samples discussed in the text are shown on the southern ridge. The bathymetric profile along cross section A-A′ is shown in Figures 9 and 10. The base map was created using Generic Mapping Tools (GMT) software [*Wessel and Smith*, 1998].

C2n (1.77–1.95 Ma [*Cande and Kent*, 1995]) [*Gee and Blackman*, 2004; *Blackman et al.*, 2006].

[7] Hole U1309D penetrated 1415.5 m below the seafloor (mbsf) with 74% recovery; 770 igneous units were recorded within this multiply intruded predominately gabbroic core, representing one of the longest, most continuous and complete in situ sections of plutonic oceanic crust ever sampled. The 1.4 km section appears to be wholly igneous crust, with limited evidence for fault related crystal-plastic deformation. Brittle deformation is confined to intervals less than a few meters thick (Figure 2).

[8] In contrast to surface sampling on the southern ridge, drilling recovered predominantly gabbroic rock types (Figure 2). Eighty-four percent of the core comprised gabbro, gabbronorite, and olivine gabbro, with lesser proportions of Fe-Ti oxide gabbro (7%), diabase (3%), ultramafic rocks (~5%), and felsic dikes (<1%). The gabbroic rocks from U1309D are grouped here into three lithostratigraphic macrounits (or lithologic supergroups I, II and III; Figure 2) based on major element chemistry and rock type, and may represent distinct intrusive series roughly 500–600 m thick [*Johnson et al.*, 2005; *Blackman et al.*, 2006]. However, in detail, the lithostratigraphy is far more complicated with dozens of interfingering Fe-Ti oxide gabbro, gabbro, olivine gabbro and troctolite intervals [*Blackman et al.*, 2006; *John et al.*, 2006].

[9] The uppermost lithologic supergroup extends from the seafloor to 600 mbsf, below which there is an abrupt change in the whole-rock Mg # toward more Fe-rich compositions (Figure 2b). Evolved Fe-Ti oxide gabbro intervals are concentrated below this boundary from 600–680 mbsf, and may represent the fractionated top of an underlying intrusive series. Whole-rock Mg # increases down section from 600 to ~1235 mbsf, culminating in a thick interval of olivine-rich troctolite between ~1090 and 1236 mbsf. Concentrations of Fe-Ti oxide gabbro dikes are observed between 1170 and 1270 mbsf, similar to below the lithologic break at 600 mbsf. A second boundary is tentatively placed at ~1235 mbsf near the base of the ultramafic rocks. Igneous contacts within the core suggest that the lithologic supergroups are made up of smaller intrusive bodies varying from centimeters to (at most) 100–200 m [*Blackman et al.*, 2006]. More fractionated rock types including Fe-Ti oxide gabbro and felsic dikes exhibit intrusive relationships with gabbro, which in turn intrude more primitive olivine gabbros and ultramafic rocks [*John et al.*, 2006; *Ildefonse et al.*, 2007]. Diabase dikes are concentrated in the upper 130 m, but occur throughout Hole U1309D; the diabase appears to be the youngest intrusive phase as it consistently intrudes all other rock types.

[10] High strain plastic deformation is fairly restricted in U1309D, although concentrations of granulite- to amphibolite-grade shear zones do
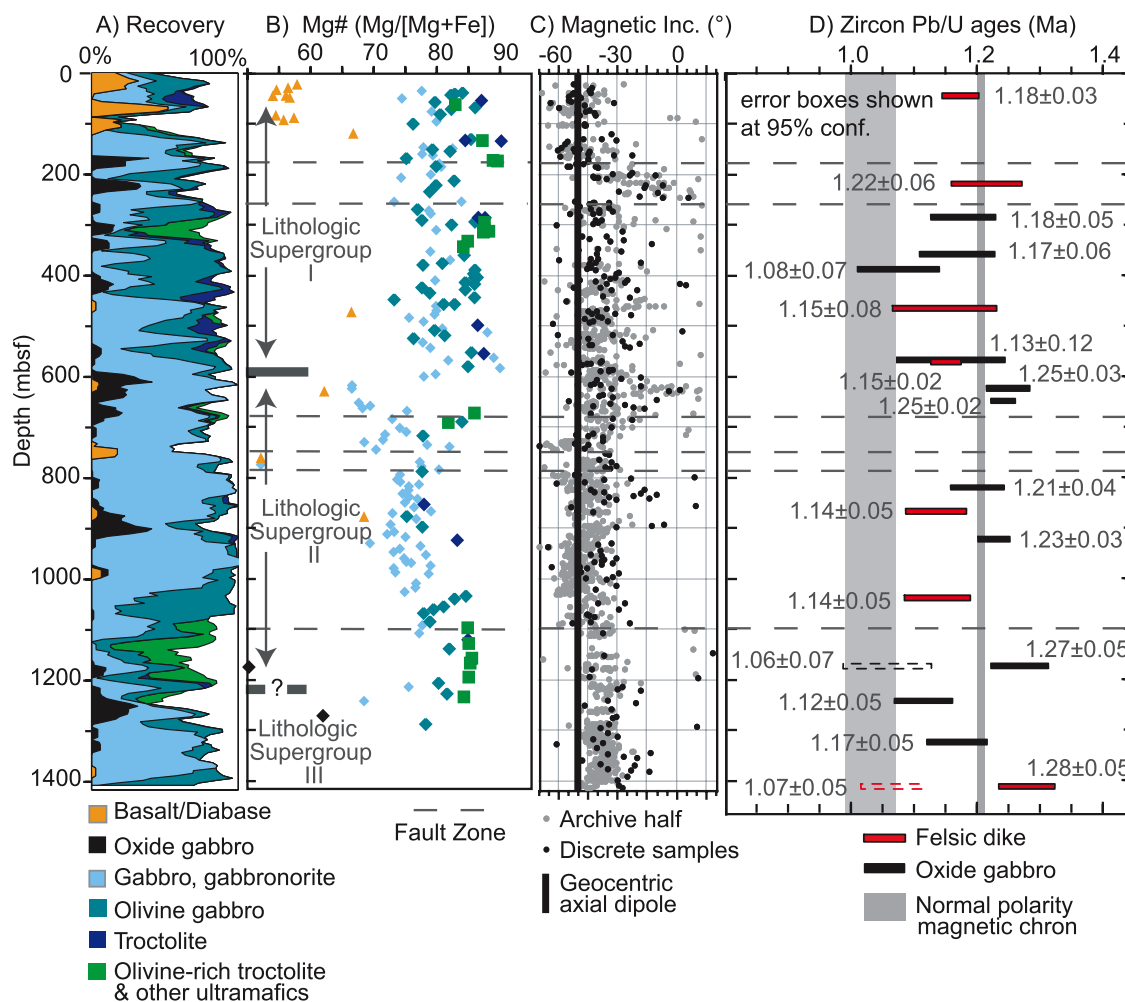
Figure 2. Plots of depth versus (a) 20 m running average of rock type recovered in Hole U1309D (white indicates no recovery), (b) whole-rock Mg #, along with inferred lithologic supergroups and fault zones, (c) magnetic inclination data for continuous measurements on the archive half of the core, and measurements from discrete samples (expected inclination at this latitude is ±49°), and (d) ^{207}Pb and ^{230}Th corrected ^{206}Pb/^{238}U sample weighted average zircon ages (shaded fields represent the Jaramillo and Cobb Mountain normal polarity intervals) [*Cande and Kent*, 1995]. Figures 2a–2c are modified from *Blackman et al.* [2006].

occur between 35 and 80 mbsf and 670–720 mbsf, and vary from millimeters up to at most a few meters in thickness [*Blackman et al.*, 2006]. Brittle deformation indicated by zones of cataclasis is also restricted, though conspicuous in several locations. Significant zones of cataclasis are observed in the upper 50 mbsf, and near 170, 250, 685–785, and 1100 mbsf (Figure 2).

[11] Downhole magnetic data collected during Expeditions 304 and 305 were used to identify 5 intervals with different magnetic inclinations (Figure 2c) [*Blackman et al.*, 2006]. Only the upper block (0–180 mbsf) gives an average inclination near the expected geocentric axial dipole for this

latitude (±49°). Deeper portions of the hole show shallower average magnetic inclinations varying from −38° to −31.5°, consistent with some tectonic rotation since cooling through the Curie temperature [*Blackman et al.*, 2006].

3. Sampling and Analytical Methods

[12] Zircon was separated from over 30 Fe-Ti oxide gabbro and felsic dike samples between 40 and 1415 mbsf in Hole U1309D. Owing to the characteristically low U content of ocean crustal zircon [*Grimes et al.*, 2007b], ages were obtained from only 18 of these to study the vertical construction of oceanic lithosphere (Figure 2d). These

18 samples represent each lithologic supergroup, structural, and magnetic inclination unit identified during shipboard investigations. Samples are named on the basis of their depth of occurrence in the hole (e.g., D40 comes from 40 mbsf in U1309D); the corresponding IODP naming convention is shown in Table 1a, with brief descriptions of each sample. In many instances, zircon was identified in thin section prior to mineral separation. In addition, 6 samples from the southern ridge (Table 1b) were dated to provide regional coverage and allow estimates of horizontal accretion rates over Atlantis Massif.

3.1. Fe-Ti Oxide Gabbro

[13] Ten samples dated from U1309D are described as Fe-Ti oxide (± amphibole) gabbro (Table 1a and Figures 2 and 3), and are named on the basis of the presence of >2% iron-titanium oxide minerals (magnetite and ilmenite) in their mode. These samples exhibit 2 types of Fe-Ti oxide enrichment. In the first and most common type, Fe-Ti oxides occur as randomly distributed patches in undeformed, coarse grained gabbro (Figure 3a) (samples D282, D355, D564, D623, D647, D820, D1245, D1327). Brown amphibole, likely igneous in origin, is associated with several of these samples. A second type of Fe-Ti oxide concentration is represented in samples D386 and D1175. These examples correspond to the type of Fe-Ti oxide gabbro defined by *Blackman et al.* [2006] as "oxide enriched gabbros near undeformed contacts" (p. 30), and are relatively uncommon. In these samples, coarse Fe-Ti oxide minerals are concentrated (up to 40% of the rock) along sharp contacts with gabbro (Figure 3b). These Fe-Ti oxide-bearing intervals are 5–10 cm thick, and contain very coarse (up to 3 cm in long dimension) Fe-Ti oxide, amphibole and/or pyroxene grains. One additional oxide-bearing gabbro sample was dated at 923 mbsf; D923 is a 10 cm thick Fe-Ti oxide-bearing gabbronorite dike with <1% Fe-Ti oxide that intrudes troctolite, and has sharp upper and lower contacts (Figure 3c). Apatite is a common accessory mineral in all samples of Fe-Ti oxide gabbro in this study, comprising up to 2% of the mode (e.g., D623). Zircon generally occurs in close association to the oxides, and/or in adjacent amphibole patches. The Fe-Ti oxide gabbros are thought to originate by local in situ fractionation of ferrobasalt melts, by analogy with those from ODP Hole 735B on the ultraslow spreading SW Indian Ridge [*Dick et al.*, 2000; *Natland and Dick*, 2002].

3.2. Felsic Dikes

[14] The felsic dikes in U1309D are centimeter-scale anorthosite, quartz diorite, and tonalite/trondjhemite leucocratic melt intrusions (Figure 3). The felsic dikes, also described as oceanic plagiogranites [*Coleman and Donato*, 1979], consist primarily of amphibole and plagioclase, and are typically overprinted by amphibolite to zeolite grade alteration that obscures original igneous mineralogy and textures. Quartz is observed in many of these samples including D215, D463, D867, D1040, and D1415. These dikes frequently host zircon and are interpreted as igneous in origin, derived from evolved silicate melts with solidus temperatures estimated between ~750 and 850°C [*Blackman et al.*, 2006]. Similar veins recovered from the gabbroic crust drilled in ODP Hole 735B are believed to have originally formed at temperatures >800°C [*Robinson et al.*, 2002], but have also been heavily overprinted by hydrothermal alteration. These temperatures are reasonably consistent with those calculated for zircon in Hole U1309D using the Ti-in-zircon thermometer [*Watson et al.*, 2006; *Ferry and Watson*, 2007], which yield sample average zircon crystallization temperatures of 764–812°C (Table 1a; *Grimes et al.* [2007b] data repository).

[15] Several possible origins for these felsic dikes have been proposed and are discussed by *Koepke et al.* [2007]. These include extreme differentiation of MORB by crystal fractionation [e.g., *Coleman and Donato*, 1979; *Aldiss*, 1981; *Niu et al.*, 2002], immiscibility in evolved tholeiitic liquids [*Natland et al.*, 1991], and anatexis of hydrated crustal gabbros [e.g., *Koepke et al.*, 2004, 2007]. In each case, the felsic melts are the final product of a thermal/magmatic event and thus the crystallization ages record emplacement of intrusive bodies, and delimit minimum accretion ages of the sampled crustal section.

3.3. Southern Ridge Samples

[16] Six additional samples from the southern wall and southeast shoulder of Atlantis Massif were also found to host zircon (Table 1b). These samples are located between 7.2 and 13 km from the peak of the present-day normal polarity magnetic epoch located near the midpoint of the axial valley [*Pariso et al.*, 1996]. These samples were collected by manned submersible and dredge during the MARVEL 2000 cruise [*Blackman et al.*, 2002; *Schroeder and John*, 2004]. Samples 3652–1333, 3652–1002, 3652–1205, and 3647–1359 were

Table 1a. Samples From IODP Hole U1309D

IODP Sample Name	Depth (mbsf)	Rock Description	Alteration	Number of Analyses	Age (Ma)	Comments	Ti-in-Zirc Temp (°C)
1309D-5R-3, Pc. 13, 136–145 cm	40	plagioclase-amphibole vein intruding gabbro	70%	14	1.18 ± 0.03		**773°** (σ = 21°, n = 15)
1309D-40R-1, Pc. 5, 21–25 cm	215	trondjhemite	5%	12	1.22 ± 0.06	rubble	**764°** (σ = 34°, n = 16)
1309D-54R-1, Pc. 6A, 52–64 cm	282	Fe-Ti oxide gabbro	30%	11	1.18 ± 0.05	10–12% Fe-Ti oxide; 1 m thick interval	
1309D-69R-2, Pc. 4A, 52–62 cm	355	Fe-Ti oxide gabbro	25%	5	1.17 ± 0.06	~1.5 m thick interval	
1309D-75R-3, Pc. 7B, 99–106 cm	386	Fe-Ti oxide gabbro	30%	5	1.08 ± 0.07	~30 cm thick interval	
1309D-93R-1, Pc. 7, 27–37 cm	463	trondjhemite intrusion zone	20%	9	1.15 ± 0.08	epidote-bearing, 50 cm thick interval	**788°** (σ = 44°, n = 10)
1309D-114R-1, Pc. 1E–1F, 62–71 cm	564	Fe-Ti oxide gabbronorite	10%	6	1.13 ± 0.12	~55 cm thick interval	
1309D-115R-2, Pc. 1D, 59–67 cm	570	Fe-Ti oxide-bearing leucocratic zone of intrusion	45%	14	1.15 ± 0.02		**812°** (σ = 34°, n = 9)
1309D-126R-2, Pc. 2B, 27–38 cm	623	Fe-Ti oxide gabbro	35%	10	1.25 ± 0.03	from ~50 m thick interval with oxide gabbros	**780°** (n = 1)
1309D-131R-2, Pc. 1, 0–10 cm	647	Fe-Ti oxide amphibole gabbro	15%	12	1.25 ± 0.02	from ~50 m thick interval with oxide gabbros	**739°** (σ = 17°, n = 5)
1309D-168R-2, Pc. 1, 0–6 cm	820	Fe-Ti oxide gabbro	25%	9	1.21 ± 0.04	~70 cm thick interval	
1309D-178R-1, Pc. 6A, 97–102 cm	867	leucocratic zone of intrusion	60%	9	1.14 ± 0.05	carbonate- and epidote-bearing	
1309D-189R-4, Pc. 3, 41–45 cm	923	gabbro (Fe-Ti oxide-bearing)	35%	9	1.23 ± 0.03	10 cm dike; intrudes troctolite	
1309D-216R-1, Pc. 3, 54–59 cm	1040	trondjhemite	30%	8	1.14 ± 0.05	2 cm thick dike; intrudes olivine gabbro	
1309D-244R-2, Pc. 5, 100–104 cm	1175	Fe-Ti oxide gabbro	15%	15	1.27 ± 0.05	~20 cm thick interval, intrudes olivine gabbro	
1309D-259R-1, Pc. 6, 22–27 cm	1245	Fe-Ti oxide gabbro	35%	11	1.12 ± 0.05		
1309D-276R-1, Pc. 6A-C, 49–65 cm	1327	Fe-Ti oxide gabbro	15%	9	1.17 ± 0.05	~30 cm thick interval	
1309D-295R-3, Pc. 1D, 100–110 cm	1415	quartz diorite	50%	14	1.28 ± 0.05	intrudes olivine gabbro	**820°** (σ = 60°, n = 10)

Table 1b. Samples From the Southern Ridge of Atlantis Massif

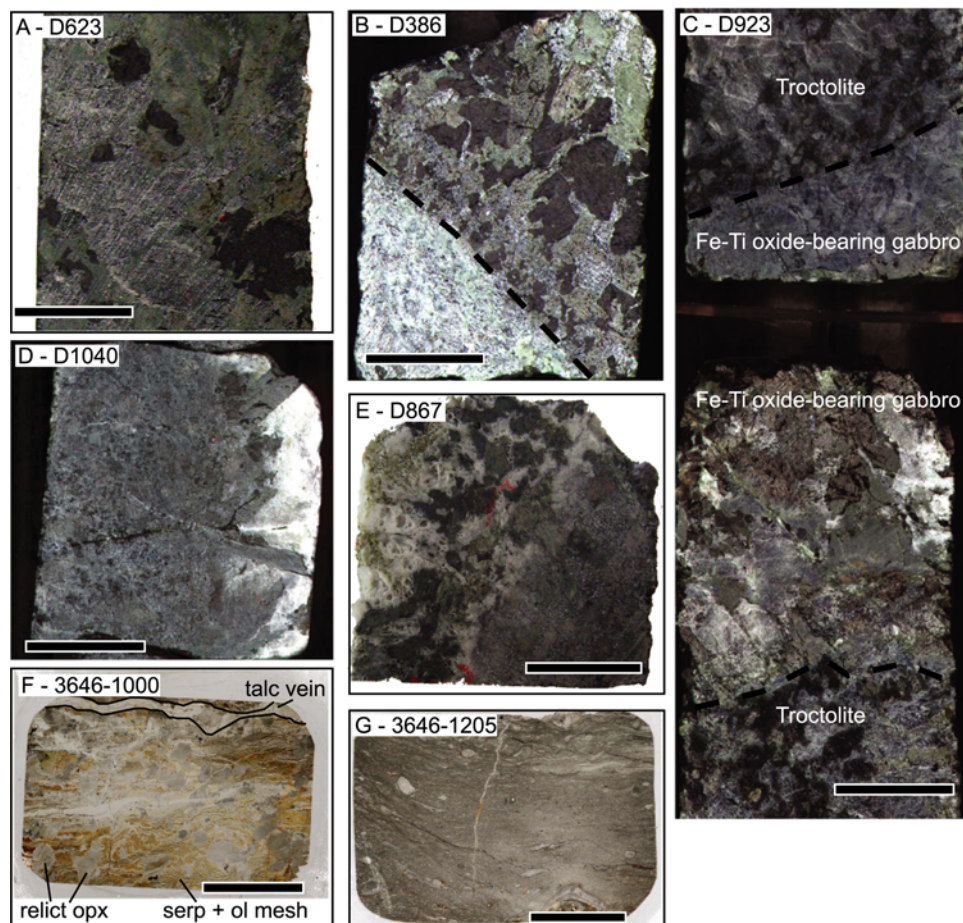|	Rock Description	Number of Analyses	Age (Ma)	Est. Distance Off-Axis (km)	Ti-in-Zirc Temp. (°C)
Alvin Dive					
3652–1333	foliated tremolite+chlorite-rich rock w/ coarse relict Fe-Ti oxide (exsolved Ti-oxide remains)	10	1.76 ± 0.04	12.8	**808°** (σ = 34°, n = 9)
3652–1002	carbonate-cemented breccia with amphibole and chlorite clasts	5	1.16 ± 0.11	13	
3646–1205	amphibole-chlorite schist	20	1.07 ± 0.03	10.6	**890°** (σ = 28°, n = 5)
3646–1000	serpentinized peridotite cut by amphibole-chlorite veins hosting zircon	8	1.13 ± 0.14	10.5	**888°** (σ = 19°, n = 6)
3647–1359	brecciated amphibole-chlorite rock with talc pseudomorphing OPX	11	0.98 ± 0.05	8.3	**870°** (σ = 63°, n = 6)
Dredge					
D3-21	metasomatized amphibole+chlorite+talc-rich fault rock w/ relict olivine & OPX	11	1.06 ± 0.10	7.2	**909°** (σ = 37°, n = 6)

Figure 3. Rock types host to zircon. (a) D623: Fe-Ti oxide gabbro with randomly distributed oxide patches, and abundant green amphibole. (b) D386: Fe-Ti oxide gabbro dike intruding gabbro with a sharp lower contact. (c) D923: Oxide-bearing gabbronorite dike intruding troctolite. (d) D1040: Trondjhemite dike intruding gabbro along the edge of recovered core. (e) D867: Leucocratic zone of intrusion with fairly sharp contact with gabbro. Clots of epidote occur in the top left. (f) 3646–1000: Serpentinized peridotite cut by thin, metasomatic veins/dikes host to zircon. (g) 3646–1205: Talc-amphibole schist. Zircon grains are distributed throughout the amphibole matrix. Scale bars 2 cm.

collected from outcrop by the submersible *Alvin*; although it is possible that some exposures recognized as outcrop from the submersible could be large talus blocks, these samples are interpreted to be collected nominally in place. In contrast, sample 3646–1000 was collected from a recognized talus block along the steep southern wall; however, the close proximity and the very similar age to 3646–1205 suggests that this sample was probably not translated far from its original location. Sample D3-21 was collected by dredge and its location is somewhat less well constrained. The samples comprise highly altered, variably deformed mafic-ultramafic rocks (Figures 3f and 3g) that were likely intruded by evolved, late-stage melts. Zircon is typically found in altered dikes/veins, but also occurs in the schistose matrix of highly deformed samples, including 3646–1205 (Figure 3f) in which more than 50 zircons are observed in one 5×8 cm thin section [*Schroeder and John*, 2004]. The most likely origin of the zircon in these samples is crystallization from an evolved gabbroic melt intruded into peridotite prior to or during deformation. Ti-in-zircon temperatures range from 810 to 910°C (Table 1b; *Grimes et al.* [2007b] data repository) and clearly indicate formation under magmatic conditions.

3.4. Mineral Separation

[17] Zircon was separated from samples weighing less than 300 g by first hand-crushing, and then grinding into <350 μm particles using a rotary disc mill. Rock flour was removed with a water bath. Iron oxides were removed using a hand magnet, followed by concentration of the high density fraction (>3.3 g/cc) using Methylene Iodide. Heavy concentrates containing fresh pyroxene or hornblende were run through a Frantz magnetic separation step at 0.5 A to further concentrate zircon. Zircon yields were variable, but many tens to hundreds of grains were commonly recovered. For each sample, approximately 20–60 grains between 40 and 150 μm in the long dimension were hand picked and mounted in epoxy, polished, and gold-coated in preparation for U-Pb isotopic analysis.

3.5. Data Collection and Reduction

[18] U-Pb dating was performed at the U.S. Geological Survey–Stanford Ion Microprobe Laboratory using the sensitive high-resolution ion microprobe–reverse geometry (SHRIMP-RG). Sample R33, a 419 Ma quartz diorite from the Braintree complex in Vermont, served as the $^{206}Pb/^{238}U$ age standard. U concentrations were calibrated using the standard CZ3, a Sri Lankan megacrystic zircon with 550 ppm U [*Ireland and Williams*, 2003]. Prior to analysis, all grains were imaged using both reflected light and cathodoluminescence (CL). The images were used as a guide for avoiding microcracks and inclusions, and for targeting grains with sufficient U concentration for high-resolution ages. U and Th concentrations are variable from 4 to >11000 ppm, but most commonly occur in low abundances of less than a few hundred ppm (Table 2). For U-Pb analyses, 5 to 20 grains were analyzed from each sample, with each spot analysis being the average of 7 scans through 9 mass stations. A spot size of $\sim$25 microns was sputtered using a $\sim$6–7 nA O^{2-} primary beam. The primary beam was rastered over the spot for 180 s prior to analysis to remove surficial common Pb. Raw data for the standard and unknowns were reduced using SQUID [*Ludwig*, 2001], and reduced data was plotted using the Excel Add-In, Isoplot v. 3.00 [*Ludwig*, 2003]. A correction for common Pb was made using the ^{207}Pb method [*Ireland and Williams*, 2003], and an age appropriate model Pb composition [*Stacey and Kramers*, 1975].

[19] An additional correction has been made to adjust for initial ^{238}U-^{230}Th disequilibrium using the equations of *Parrish and Noble* [2003]. Zircons commonly incorporate U preferentially over Th, leading to U series secular disequilibrium during crystallization (due to exclusion of the ^{238}U series intermediate daughter, ^{230}Th) resulting in a deficit of radiogenic ^{206}Pb. Correcting for this disequilibrium requires knowledge of the Th/U, and common Pb corrected $^{206}Pb/^{238}U$ ratios of the zircon grain, and the Th/U ratio of the magma ($[Th/U]_{magma}$) at the time of zircon crystallization. The latter is not known, but a $[Th/U]_{magma} = 3$ is estimated on the basis of the mean value for MAR basalts (data downloaded from PETDB.org, 7/07). The correction results in calculated ages that (on average) are older by $\sim$70 ka ($\sim$6%). Although the $[Th/U]_{magma}$ value is estimated, large differences in $[Th/U]_{magma}$ result in relatively small differences in the calculated correction. For example, if a $[Th/U]_{magma}$ ratio of 2 or 4 is used the resulting correction would differ by <20 ka for the relevant ages, and corresponds to a $\sim$2% uncertainty in the absolute age of samples from Atlantis Massif. The secular disequilibrium correction shifts all weighted average ages to slightly older values, and therefore has

Table 2. (Sample). Isotopic Age Data [The full Table 1 is available in the HTML version of this article at http://www.g-cubed.org.]

Sample Grain	Concentrations U (ppm)	Th (ppm)	^{206}Pb[b] (ppm)	f_{206}[c] (%)	Atomic Ratios[a] ^{238}U/^{206}Pb[d] (abs err)	^{207}Pb/^{206}Pb[d] (abs err)	^{207}Pb corrected ^{206}Pb/^{238}U[e] (abs err)	^{207}Pb Corrected Ages (Ma) ^{206}Pb/^{238}U[f] (1σ)	Weighted Average (2σ)	^{230}Th Corrected (errors 2σ, abs) ^{206}Pb/^{238}U[e]	^{206}Pb/^{238}U[f]	Weighted Average Age (Ma)
IODP Hole 1309D												
D40-1	508	329	0.09	12.9	4986 ± 235	0.1476 ± 0.0183	0.000175 ± 0.000009	1.13 ± 0.06	1.10 ± 0.03	0.000188 ± 0.000019	1.21 ± 0.12	**1.18 ± 0.03**
D40-2	631	340	0.10	9.0	5526 ± 244	0.1173 ± 0.0146	0.000165 ± 0.000008	1.06 ± 0.05	MSWD = 0.31	0.000178 ± 0.000016	1.15 ± 0.10	**MSWD = 0.21**
D40-3	612	279	0.09	8.8	5615 ± 272	0.1158 ± 0.0178	0.000162 ± 0.000009	1.05 ± 0.06		0.000177 ± 0.000018	1.14 ± 0.11	
D40-4	551	295	0.09	12.2	5311 ± 259	0.1422 ± 0.0181	0.000165 ± 0.000009	1.07 ± 0.06		0.000179 ± 0.000018	1.16 ± 0.12	
D40-5	528	328	0.07	11.2	6383 ± 348	0.1347 ± 0.0207	0.000139 ± 0.000009	0.90 ± 0.06		0.000152 ± 0.000017	*0.98 ± 0.11*	
D40-6	619	383	0.10	12.3	5124 ± 234	0.1428 ± 0.0174	0.000171 ± 0.000009	1.10 ± 0.06		0.000185 ± 0.000018	1.19 ± 0.12	
D40-7	1014	636	0.16	8.4	5392 ± 211	0.1124 ± 0.0121	0.000170 ± 0.000007	1.09 ± 0.05		0.000183 ± 0.000014	1.18 ± 0.09	
D40-8	1211	854	0.19	8.7	5522 ± 198	0.1147 ± 0.0108	0.000165 ± 0.000006	1.07 ± 0.04		0.000178 ± 0.000013	1.15 ± 0.08	
D40-9	1036	762	0.17	8.5	5309 ± 203	0.1129 ± 0.0114	0.000172 ± 0.000007	1.11 ± 0.05		0.000185 ± 0.000014	1.19 ± 0.09	
D40-10	658	291	0.10	6.9	5468 ± 247	0.1005 ± 0.0140	0.000170 ± 0.000008	1.10 ± 0.05		0.000185 ± 0.000017	1.19 ± 0.11	
D40-11	767	463	1.15	87.9	575 ± 78	0.7406 ± 0.0507	0.000210 ± 0.000119	1.35 ± 0.77		0.000223 ± 0.000238	1.44 ± 1.53	
D40-12	1348	1865	0.23	12.6	5004 ± 175	0.1454 ± 0.0123	0.000175 ± 0.000007	1.13 ± 0.04		0.000184 ± 0.000014	1.18 ± 0.09	
D40-13	550	209	0.09	12.4	5197 ± 261	0.1438 ± 0.0192	0.000169 ± 0.000010	1.09 ± 0.06		0.000183 ± 0.000019	1.18 ± 0.12	
D40-14	1641	1711	0.26	4.3	5418 ± 210	0.0802 ± 0.0106	0.000177 ± 0.000007	1.14 ± 0.05		0.000187 ± 0.000015	1.21 ± 0.09	
D215-1	220	117	0.04	12.4	4961 ± 371	0.1441 ± 0.0304	0.000177 ± 0.000015	1.14 ± 0.10	1.13 ± 0.06	0.000190 ± 0.000031	1.23 ± 0.20	**1.22 ± 0.06**
D215-2	402	292	0.07	5.5	5236 ± 317	0.0893 ± 0.0211	0.000181 ± 0.000012	1.16 ± 0.08	MSWD = 2.4	0.000193 ± 0.000024	1.25 ± 0.16	**MSWD = 2.6**
D215-3	260	142	0.04	11.6	5047 ± 349	0.1374 ± 0.0269	0.000175 ± 0.000014	1.13 ± 0.09		0.000189 ± 0.000028	1.22 ± 0.18	
D215-4	253	147	0.04	14.9	5102 ± 362	0.1636 ± 0.0301	0.000167 ± 0.000014	1.08 ± 0.09		0.000180 ± 0.000028	1.16 ± 0.18	
D215-5	319	170	0.05	12.2	5709 ± 376	0.1423 ± 0.0253	0.000154 ± 0.000012	0.99 ± 0.07		0.000168 ± 0.000023	1.08 ± 0.15	
D215-6	1220	589	0.23	16.8	4630 ± 168	0.1784 ± 0.0141	0.000180 ± 0.000008	1.16 ± 0.05		0.000194 ± 0.000015	1.25 ± 0.10	
D215-7	1129	1268	0.34	55.6	2847 ± 86	0.4854 ± 0.0199	0.000156 ± 0.000011	1.00 ± 0.07		0.000166 ± 0.000021	1.07 ± 0.14	
D215-8	1520	1491	0.42	46.6	3084 ± 175	0.4141 ± 0.0238	0.000173 ± 0.000014	1.12 ± 0.09		0.000184 ± 0.000028	1.19 ± 0.18	
D215-9	1044	890	0.19	7.1	4648 ± 185	0.1019 ± 0.0131	0.000200 ± 0.000009	1.29 ± 0.06		0.000212 ± 0.000017	1.37 ± 0.11	
D215-10	2175	1065	0.36	4.1	5172 ± 160	0.0783 ± 0.0072	0.000185 ± 0.000006	1.20 ± 0.04		0.000200 ± 0.000012	1.29 ± 0.08	
D215-11	995	838	0.17	24.2	4951 ± 203	0.2374 ± 0.0197	0.000153 ± 0.000008	0.99 ± 0.05		0.000165 ± 0.000016	1.07 ± 0.10	
D215-12	1069	220	0.18	7.1	5191 ± 200	0.1022 ± 0.0114	0.000179 ± 0.000007	1.15 ± 0.05		0.000195 ± 0.000015	1.26 ± 0.10	
D282-1	452	287	0.08	7.6	5106 ± 242	0.1064 ± 0.0163	0.000181 ± 0.000009	1.17 ± 0.06	1.10 ± 0.05	0.000194 ± 0.000019	1.25 ± 0.12	**1.18 ± 0.05**
D282-2.1	1336	791	0.22	3.5	5294 ± 144	0.0739 ± 0.0080	0.000182 ± 0.000005	1.17 ± 0.03	MSWD = 2.0	0.000196 ± 0.000011	1.26 ± 0.07	**MSWD = 2.1**

[a] Errors reported at 1σ.
[b] Radiogenic ^{206}Pb.
[c] Fraction of ^{206}Pb that is common.
[d] Uncorrected, measured ratios.
[e] The ^{207}Pb corrected ratios using age appropriate model Pb isotopic composition of *Stacey and Kramers* [1975].
[f] The ^{207}Pb corrected age. Spot analyses in italics either were identified as outliers (from concordia diagrams) or contained more than 5000 ppm U, and were excluded from the mean age.

little effect on the relative age differences between samples.

[20] Zircon trace element geochemistry has also been collected for samples in this study using the SHRIMP-RG following the methods described by *Mazdab and Wooden* [2006] (see also *Grimes et al.* [2007b] data repository). The results of those analyses are discussed elsewhere [*Grimes et al.*, 2007b]; however, temperature estimates have been determined from the measured Ti concentrations using the Ti-in-zircon thermometer of *Watson et al.* [2006] and are reported in Tables 1a and 1b. Temperatures have been calculated using the revised thermodynamic calibrations of *Ferry and Watson* [2007]. Owing to the absence of rutile in these rocks (indicating $a_{TiO2} < 1$) a correction has been applied using an estimated $a_{TiO2} = 0.7$, appropriate for the presence of Fe-Ti oxides and titanite [e.g., *Claiborne et al.*, 2006]. The a_{SiO2} is assumed to be 1 on the basis of the presence of quartz in several host rocks, and quartz inclusions in numerous zircon grains.

3.6. Zircon Morphology

[21] Recovered zircons are subdivided into three types on the basis of clarity, internal and external textures, and morphology. Type 1 grains are colorless, euhedral, faceted, gem quality grains with aspect ratios varying from 1:1 to 4:1. In thin section, grain sizes range from 5 μm up to 1.5 mm. Type 2 grains are similar in size and clarity, but occur as subhedral to anhedral crystals, and are typically recovered from Fe-Ti oxide gabbro. These grains likely result from late-stage crystallization in interstitial melt pockets [*Scoates and Chamberlain*, 1995], resulting in inhibited growth and irregular crystal development. Alternatively, some type 2 grains might simply be fragments of type 1 grains resulting from the mineral separation process. Faint oscillatory and sector zoning patterns typical of igneous zircon [*Hanchar and Miller*, 1993; *Hoskin and Schaltegger*, 2003; *Corfu et al.*, 2003] are observed for both types 1 and 2 using CL (refer to Figure 4). Type 1 and 2 grains are interpreted as igneous on the basis of these textures, and have sample-average Ti-in-zircon temperatures between 739 and 909°C (Tables 1a and 1b). By contrast, type 3 grains are opaque, faintly colored (pinkish, or yellow to brown), exhibit convoluted zoning patterns, and may contain pores up to 10 μm in diameter, as well as 1–2 micron Th, U, and/or Hf-rich inclusions. Porous domains also occur in what otherwise appear to be normal type 1 and 2 grains. Similar textural characteristics are described for altered zircons from continental crust that may have undergone fluid-assisted dissolution-reprecipitation reactions [e.g., *Geisler et al.*, 2007]. Ti-in-zircon temperatures from these domains vary between 700 and >1000°C, but may be unreliable owing to overlapping of the ion beam with porous domains that may contain non-structural elements including Ti. This possibility also indicates the need for caution when interpreting Pb/U isotopic ages for the porous domains, as common Pb could be retained in the pores. Therefore, age analysis of grains with porous domains is restricted to the two samples discussed in section 4.

4. Results

[22] Zircon ages for 239 grains from 24 samples of ocean crust are listed in Table 2. Weighted average ages for samples from Hole U1309D range from 1.08 ± 0.07 Ma to 1.28 ± 0.05 Ma, spanning ~200 (±120) ka. Measured, uncorrected isotopic ratios are plotted on Tera-Wasserburg concordia diagrams [*Tera and Wasserburg*, 1972] in Figures 4 and Figure 5. Data for each sample are plotted on Tera-Wasserburg concordia instead of conventional concordia owing to the young age, and therefore extremely low abundances of radiogenic [207]Pb. Concordia diagrams afford visual evaluation of coherency of spot analyses within a sample and identification of potential outliers, but are not used here to determine ages directly. All ages quoted throughout the text are [207]Pb and [230]Th corrected weighted average [206]Pb/[238]U ages (Table 2). Errors range from ±20 to ±120 ka and are presented at the 95% confidence level.

[23] The ages determined for all type 1 and 2 zircons are taken to indicate the timing of igneous zircon crystallization (Figure 4). The solidus temperature for Fe-Ti oxide gabbros is not well constrained, although studies of gabbros with similar modal and chemical composition from Atlantis Bank have yielded an upper estimate of ~900°C using oxide pairs in symplectic intergrowth with pyroxene [*Natland et al.*, 1991]. *Botcharnikov et al.* [2008] report a ferrogabbro solidus temperature under water-saturated conditions of ~820°C based on melting experiments on the hydrous ferrogabbro system. *Coogan et al.* [2001] estimate the solidus temperature of gabbros from the Mid-Atlantic Ridge using amphibole-plagioclase thermometry to be ~860 ± 30°C. Solidus temperatures for felsic dikes sampled at the Atlantis Bank core complex
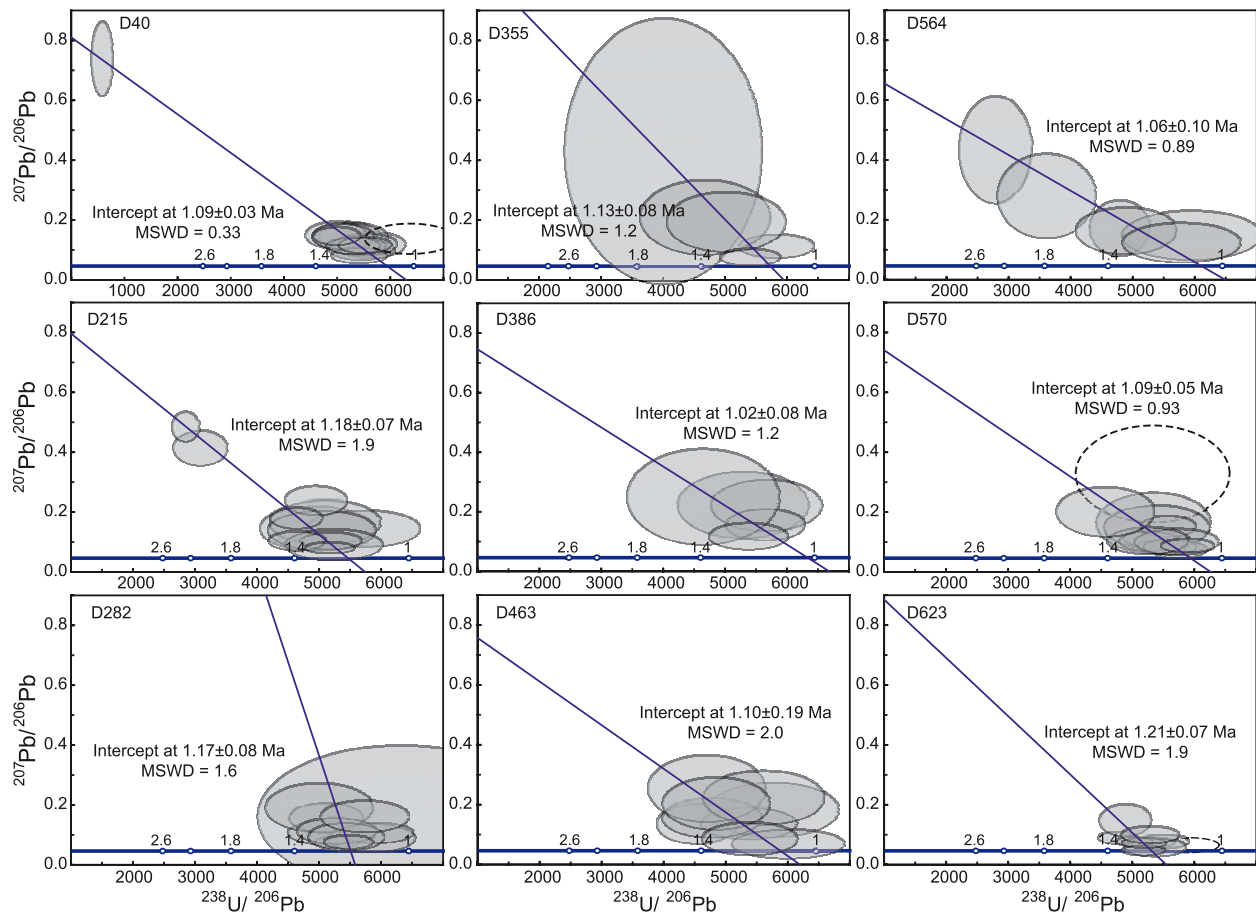
Figure 4. Tera-Wasserburg concordia diagrams showing all grains analyzed from Hole U1309D and samples collected on the surface of Atlantis Massif. The spot analyses for most samples cluster on or slightly above concordia or are pulled up a single regression line, indicating mixing with an initial component of common Pb. The mean square of weighted deviates (MSWD) values are typically near (or less than) 1.0, indicating that the observed scatter in the data can be attributed to the assigned errors defined by analytical uncertainties [*Ludwig*, 2003]. Analyses shown as dashed error ellipses were excluded from determination of the weighted average ages owing to potential open-system behavior (Pb loss), large errors, and/or high U. Grains with U concentrations greater than ~3000 ppm are excluded because such high U has been observed to cause matrix effects that can lead to an overestimate of the Pb/U ratio measured using secondary ion mass spectrometry (SIMS) [*Williams and Hergt*, 2000].

(SWIR) are estimated between ~750 and >800°C on the basis of amphibole-plagioclase thermometry [*Robinson et al.*, 2002]. On the basis of crystallization temperature estimates of ocean zircon determined using the Ti-in-zircon thermometer (739–909°C, Tables 1a and 1b [*Coogan and Hinton*, 2006; *Grimes et al.*, 2007b]), we therefore interpret the zircon ages as recording the timing of late-stage crystallization at near-solidus conditions rather than the age of melt intrusion. Cooling rates determined for lower oceanic crust from Ca-in-olivine geospeedometry, thermochronometry, and thermal modeling experiments range from ~10^3–10^4 °C/Ma [*Coogan et al.*, 2002; *John et al.*, 2004; *Maclennan et al.*, 2005]. These rates imply a time difference between the emplacement of

gabbro (>1000°C) and the crystallization of zircon (~800°C) of between 20 and 200 ka. We note no correlation between Ti-in-zircon temperature and Pb/U zircon age; therefore the variations in age we report are not simply a function of cooling (Figure 6).

[24] Two samples hosting both normal igneous grains and type 3 (porous) zircon, D1175 and D1415, display greater scatter on concordia diagrams and corresponding high mean square of weighted deviates (MSWD) values relative to other samples (Figure 4 and Table 2). In each case, porous domains were analyzed both intentionally and accidentally owing to overlap of the primary ion beam onto these texturally distinct areas. The statistical fit to the data from these samples is greatly improved by considering analysis on po-
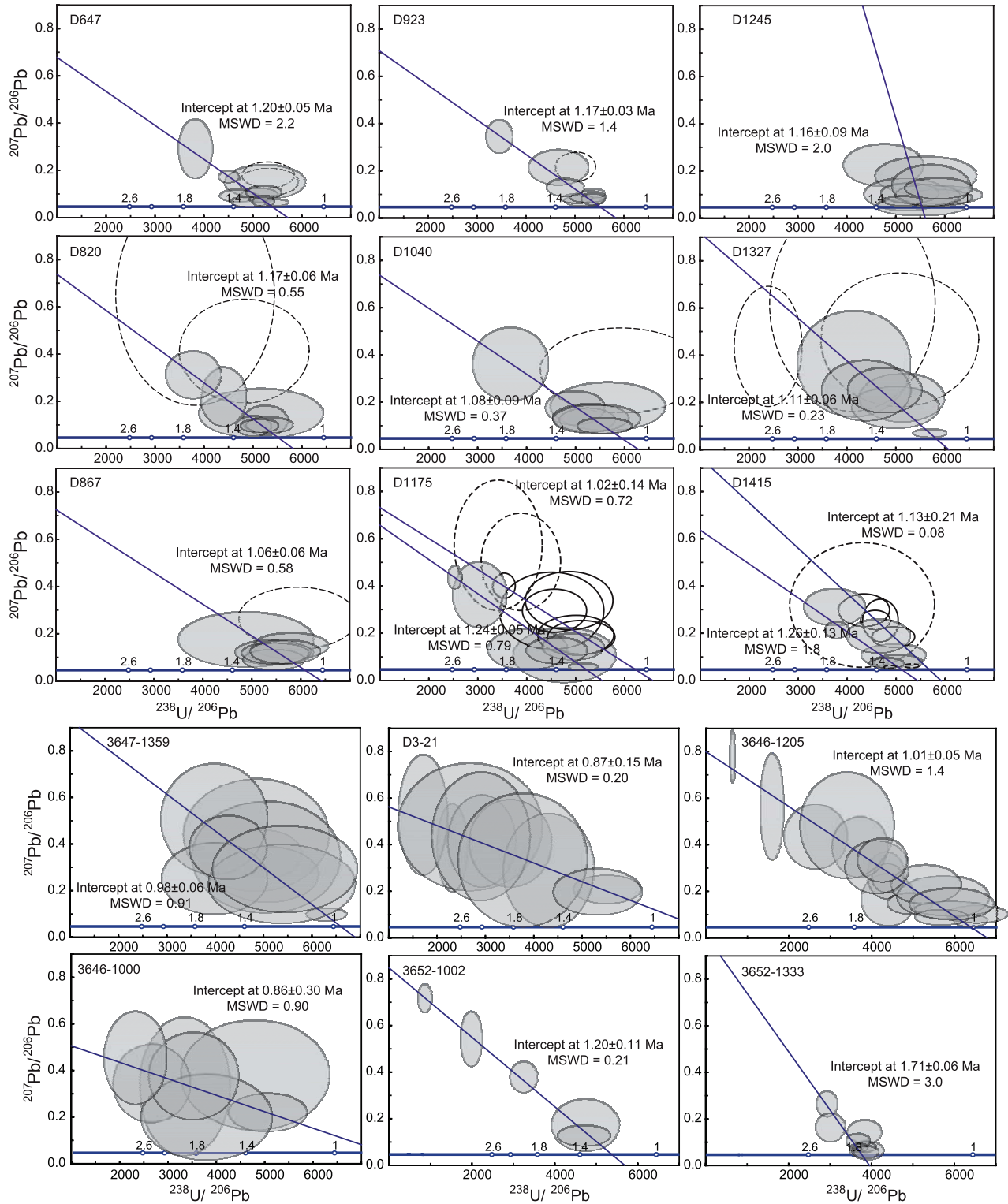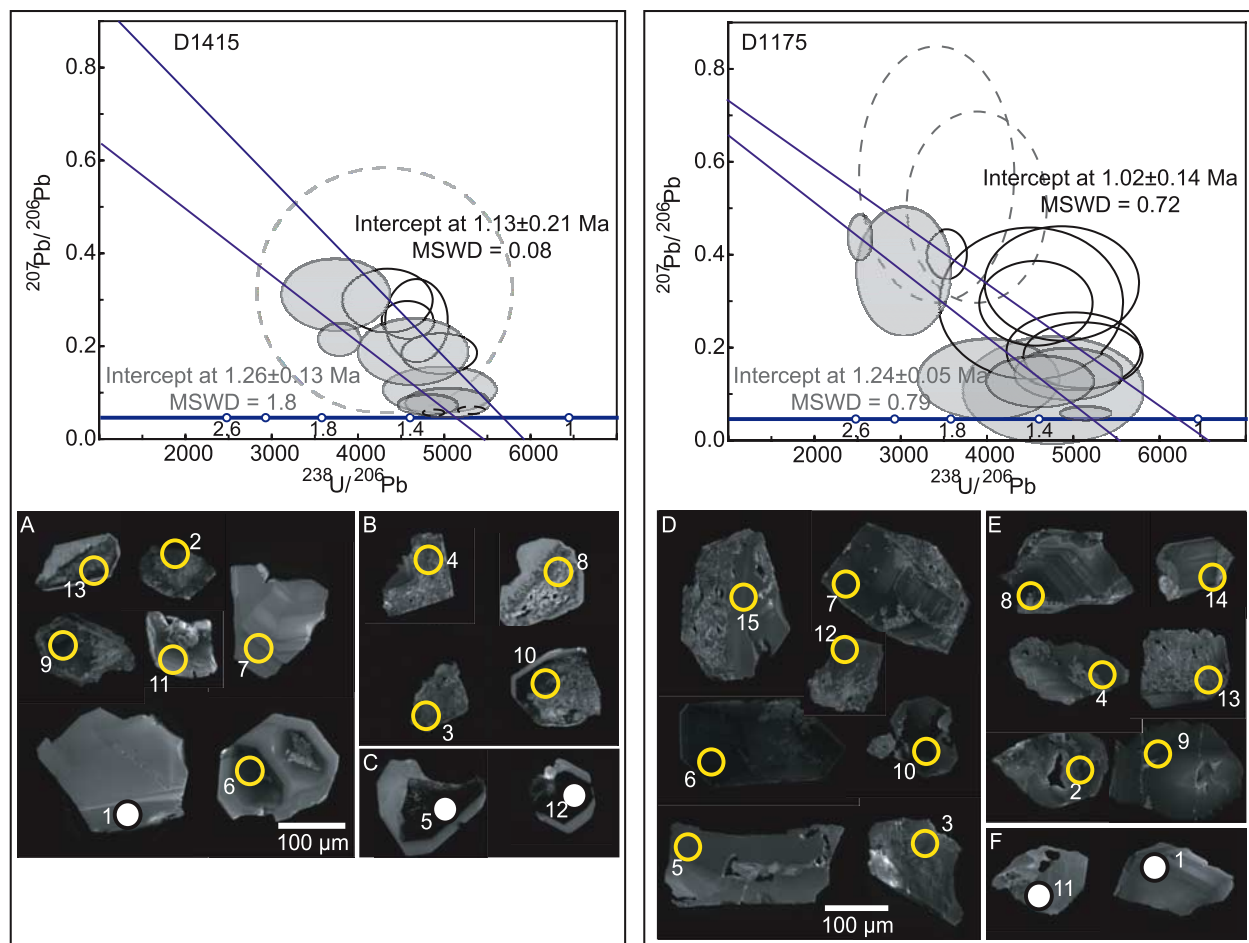
Figure 4. (continued)

Figure 5. Spot locations for isotopic age analysis of zircon in samples D1415 and D1175 and corresponding Tera-Wasserburg concordia diagrams. Numbers correspond to the analyses listed in Table 2. Sample D1415: (a) Older age population. Grains 2, 6, 9, and 11 show signs of incipient development of microporosity, but analysis spots are primarily located on domains with normal igneous zonation; spot 13 overlaps regions with both normal igneous zonation and porous character. Grain 1 is excluded from all age determinations owing to low U (34 ppm) resulting in large errors. (b) Porous grains with relatively young isotopic ages. (c) High U cores. Spots 5 and 12 were excluded from any age determinations. Sample 1175: (d) Old age population. Spots are located on primarily unaltered domains of type 1 and 2 grains. (e) Young age population. Spots overlap both normal domains and type 3 zones with microporosity. (f) Grains 1 and 11; excluded from all age determinations owing to relatively low U (59 and 75, respectively), high common Pb, and large errors. On the Tera-Wasserburg concordia diagrams, analyses grouped in the young populations are shown as open black error ellipses, and those in the old age populations are shown as gray, shaded error ellipses. Dashed error ellipses correspond to the filled white spot locations and were excluded from age determinations.

rous domains separately, thereby assuming a bimodal age distribution (Figure 5 and Table 2).

[25] Sample D1415 is an olivine gabbro intruded by a quartz-bearing felsic dike; zircon is observed only in direct association with the felsic dike. The weighted average age of 10 spot analyses (excluding 1 grain with only 34 ppm U and 2 grains with >5000 ppm U, Figure 5) is 1.20 ± 0.08 Ma, with an MSWD = 4.0 (probability of fit = 0.0) (Table 2). The high MSWD reflects significant scatter in the data that cannot be explained by analytical uncer-

tainties alone. Considering analyses from only 6 non-porous spots (Figure 5a), we calculate an age of 1.28 ± 0.05 Ma with an improved MSWD of 0.51. Spot analyses from the 4 porous grains (Figure 5b) give an age of 1.08 ± 0.05 Ma (MSWD = 0.23).

[26] Sample D1175 is a Fe-Ti oxide gabbro intrusive into olivine gabbro; the weighted average age of 13 spot analyses is 1.20 ± 0.07 Ma, with an MSWD = 2.9 (probability of fit = 0.0) (Table 2). Several spots analyzed on grains from D1175 clearly overlap both pristine and porous areas
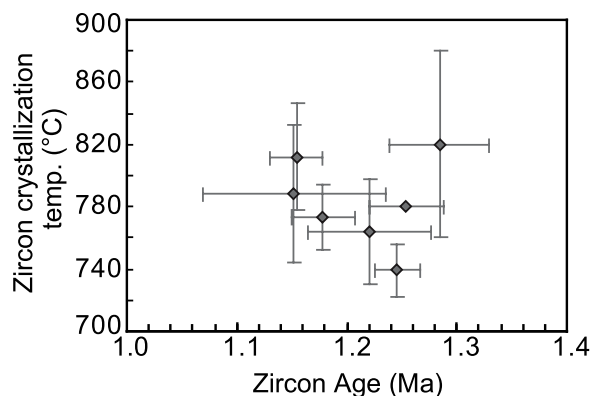
Figure 6. Zircon age versus Ti-in-zircon crystallization temperature. The lack of correlation implies that age differences are not the result of cooling. Uncertainties in temperature are given as the standard deviation of the suite of zircons in a given sample.

(Figure 5); therefore, a distinction based on textures alone is not as straightforward as in sample D1415. However, by considering spot locations along with the isotopic data, we again interpret two age populations. Seven analyses on mostly non-porous domains (Figure 5d) yield an older age of 1.27 ± 0.05 Ma (MSWD = 0.67). Six younger spot analyses that in part overlap porous domains (Figure 5e) give a mean age of 1.06 ± 0.07 Ma (MSWD = 1.0). We note that these ages are not within error, and have much improved MSWDs. We also note that the both the young age and old age determined for D1415 and D1175 are nearly identical.

[27] In both samples discussed (D1175 and D1415), the older age determined from spot analyses on relatively pristine domains of the grains is interpreted as the best estimate of the crystallization age of this sample. The younger age is clearly related to the porous domains and may represent one or more of the following events including the timing of growth/development of the porous domains, or Pb loss due to local reheating by a nearby younger intrusion, partial dissolution/reprecipitation, or during deuteric alteration by exsolved magmatic fluids. It is not clear what these porous domains represent, so their age is presented with a high degree of caution. As our focus here is the timing of igneous crystallization, the younger ages are excluded, and the older age is considered the most robust estimate of the emplacement age of the rocks in which they occur.

4.1. Age of Hole U1309D

[28] The weighted mean for all 18 samples dated in Hole U1309D is 1.20 ± 0.03 Ma (MSWD = 7.1). However, age differences are resolvable throughout the crustal section and between rocks of similar composition; this observation explains the high MSWD value for the mean age from all the samples. The age variation we see, therefore represents real temporal variation, and is not consistent with emplacement of the entire section by one short-lived (tens of ka) period of accretion.

[29] Eight ages were determined in lithologic supergroup I (0–600 mbsf) from samples of both Fe-Ti oxide gabbro and felsic dikes. These ages are within error, barring sample D386 that appears to be younger, and is not within error of D40 and D215. Excluding D386, the weighted average age for the remaining 7 samples is 1.17 ± 0.02 Ma (MSWD = 1.03) (Figure 7). Sample D386 has the youngest age of the samples from this interval; it was sampled from a 30 cm thick oxide-rich dike that exhibits a very sharp lower intrusive contact into gabbro (Figure 3b). With an age of 1.08 ± 0.07 (MSWD = 1.04), D386 represents the youngest crystallization event sampled in U1309D.

[30] Within lithologic supergroup II (600–1235 mbsf), zircon ages define two age populations that correlate to rock type. In this interval, ages from the 5 Fe-Ti oxide gabbro samples are within error (Table 2), and taken together yield a weighted average age of 1.24 ± 0.02 Ma (MSWD = 1.6) (Figure 7). Two felsic dikes yield nearly identical ages of 1.14 ± 0.05 Ma, and are distinctly younger than the Fe-Ti oxide gabbros throughout this interval. The age of the felsic dikes are indistinguishable from the samples in lithologic supergroup I.

[31] Ages for the 3 samples from the deepest ~250 m of Hole U1309D are variable and also represent two periods of zircon crystallization. A felsic dike at 1415 mbsf gives the oldest age observed in the Hole (1.28 ± 0.05 Ma), although we note this age is within error of the Fe-Ti oxide gabbros between 600 and 1235 mbsf. In contrast, the Fe-Ti oxide gabbro sampled at 1245 and 1327 give ages of 1.12 ± 0.05 Ma (MSWD = 0.99) and 1.17 ± 0.05 Ma (MSWD = 1.3). The ages do not overlap with the crystallization age determined for D1415 or the mean age of the overlying Fe-Ti oxide gabbros between 600 and 1235 mbsf; however, they are similar to the felsic dike samples of lithologic supergroup II and the weighted average age determined from 7 samples in lithologic supergroup I.
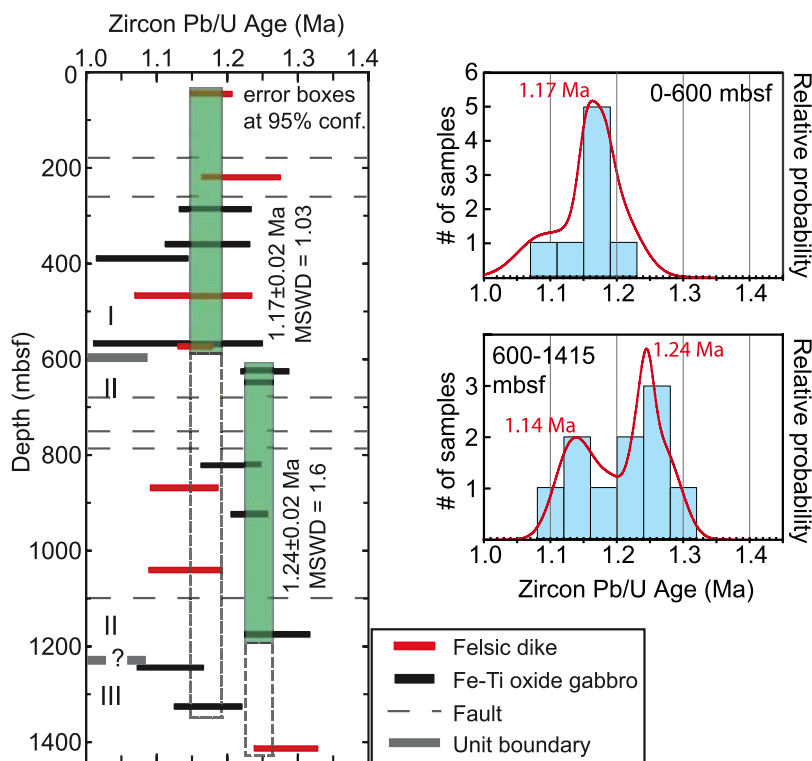
Figure 7. Interpretation of coherent age blocks in Hole U1309D. Core observations suggest these thicker intervals showing coherent ages are constructed by many smaller, interfingering intrusions. However, the age data constrain the broad-scale age progression throughout the core and indicate at least two major periods of intrusive activity, with a younger event focused above 600 mbsf at ~1.17 Ma and an older event focused between 600 and 1200 at ~1.24 Ma. Relative probability density plots [*Ludwig*, 2003] are shown for two depth intervals and highlight the presence of a single age peak above 600 mbsf, in contrast to two distinct age peaks below 600 mbsf.

Relative probability density histograms of all the age data show two well-defined age peaks below 600 mbsf, in contrast to only one age peak above 600 mbsf (Figure 7).

4.2. Southern Ridge Samples

[32] Six samples collected from the southern region of Atlantis Massif (Figure 1) yielded zircon analyzed in this study. These samples have ages between 0.98 ± 0.05 Ma and 1.76 ± 0.03 Ma (Table 2), and become older further from the ridge as predicted by simple seafloor spreading. Sample 3652–1333 is significantly older than expected relative to the other samples and its distance off-axis. Explanations for the anomalously old age of sample 3652–1333 are explored in section 5.3. Sample D3-21 is the only sample collected by dredging and therefore has a greater uncertainty in location compared to the other samples that were collected from outcrop by submersible. D3-21 was collected on the east-facing slope of the southeast shoulder adjacent to the ridge axis (see Figure 1),

and could have slumped toward the axial valley. The distance this sample was collected from the ridge axis is therefore interpreted as a minimum estimate of emplacement; the sample could conceivably have originated from as far away as the break in slope ~1.5 km upslope (above sample 3647–1359 in Figure 1). The error placed on the off-axis distance for this sample is therefore larger than for other samples, and asymmetrically distributed.

5. Discussion

[33] Pb/U zircon ages from IODP Hole U1309D taken with others spaced broadly across the southern ridge of Atlantis Massif afford the unique opportunity to address processes of crustal accretion (absolute timing, duration and patterns of magma emplacement), as well as the partitioning of extension between magmatic and tectonic processes in an oceanic core complex.

5.1. Protracted Vertical Accretion at Atlantis Massif

[34] Core observations and whole-rock geochemistry demonstrate that the gabbroic section sampled at Atlantis Massif had a complicated intrusive history and was built by multiple intrusive events [*Johnson et al.*, 2005; *Blackman et al.*, 2006; *John et al.*, 2006]. The zircon age distribution outlined above resolves at least two periods of Fe-Ti oxide gabbro and felsic dike crystallization within the section (Figure 7). The older event at ~1.24 Ma is confined to the bottom part of the recovered section (below 600 m) and appears absent from the uppermost 600 m of the core. The deepest sample at 1415 mbsf is the oldest in the hole, but is within error of the oxide gabbros dated between 600 and 1235 mbsf making it difficult to rule out the possibility that the section was originally contiguous, and subsequently cut by interfingering magmatic intrusions that expanded/inflated the section. The younger event centered around 1.17 Ma occurs throughout the core.

[35] We suggest that the older crystallization ages correlate with the intrusive events that led to formation of the majority of lithologic supergroup II. The younger zircon ages correlate with the intrusive events that led to the formation of supergroup I, and possibly the evolved gabbros at ~1240–1330 mbsf in supergroup III. The 4 young ages recorded by felsic dikes and Fe-Ti oxide gabbros in supergroups II and III (Figure 7) could then represent the interfingering of gabbro emplaced contemporaneously with the formation of supergroup I. Alternatively, these samples could have been emplaced in association with the intrusion of a third sill-like body intruding below, and into, supergroup II. The latter interpretation is supported somewhat by the weighted mean age for these 4 younger samples below 600 mbsf of 1.14 ± 0.02 (MSWD = 0.88), which is slightly younger than the age of lithologic supergroup 1. However, the mean ages for both lithologic supergroup 1 and the young samples below 600 mbsf are within error, and so either interpretation is viable. These two distinct periods of magmatism suggest that major intrusive activity was episodic on the scale of at least 70,000 a (Figure 7).

[36] The geochronologic data are broadly consistent with a simple two stage intrusive history, but do not resolve the complete temporal history of construction of each supergroup. Detailed core observations reveal over 250 demonstrable intrusive igneous contacts throughout U1309D, implying an average unit thickness of ~10 m (B. John, personal communication, 2007). We therefore infer growth of each supergroup by accretion of ~10 m scale bodies of magma over relatively short timescales. Considering supergroup II, the 5 Fe-Ti oxide gabbro samples have ages that are the same within error, but the errors allow the duration of emplacement to be as great as 150 ka (the errors allow D1175 to be as old as 1.32 Ma, and D820 to be as young as 1.17 Ma). Using these estimates to constrain the duration of vertical accretion, crust between 600 and 1235 mbsf would have accreted by the emplacement of one 10 m thick sill roughly every 2400 years, implying a minimum continuous growth rate of 0.4 cm/a. However, given the recognition of two episodes of intrusive activity, and assuming 40,000 year duration for each pulse (based on the 95% confidence interval for the mean age of each intrusive pulse shown as shaded boxes in Figure 7), crust between 600 and 1235 mbsf would have accreted by emplacement of one 10 m thick sill every 630 years, implying a continuous growth rate of 1.6 cm/a.

5.2. Effect of Faulting and Rotation on the Age Distribution

[37] Faulting (both ductile and brittle) and consequent rotation of the footwall to the detachment fault could alter the primary distribution of ages resulting from magmatic emplacement of the gabbroic section recovered at Atlantis Massif. There are two possible complications. First, faults and shear zones might have led to juxtaposition of crustal sections with differing ages. Second, fault related counterclockwise rotation could lead to apparent younging upward age relationships.

[38] No appreciable offset in age is noted across the fault zones recognized in Hole U1309D (Figure 2), and likewise no faults have been identified between samples that do exhibit significant age differences (i.e., near 600 mbsf). This implies that the fault zones within the footwall have not undergone sufficient displacement to affect the distribution of age with depth in the hole at the resolution of the geochronological data.

[39] The rolling hinge model for flexural rotation of the footwall to a large slip detachment fault allows a fault to be initiated at a high-angle (~60°), and subsequently rotate to a more gentle orientation with time and slip [*Buck*, 1988; *Tucholke and Lin*, 1994; *Lavier et al.*, 1999]. Footwall rotation would reorganize a gabbroic section of crust (and therefore the original age distribution) relative to
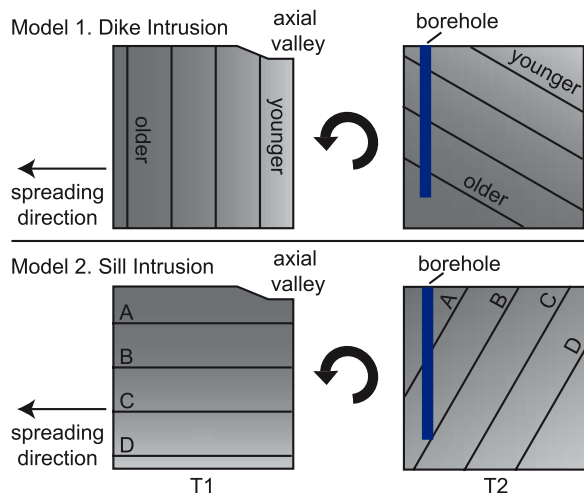
Figure 8. The effects of tectonic rotation on the geometry and distribution of rocks sampled in a borehole drilled away from the ridge axis. Model 1: Crustal accretion occurs through emplacement of vertical dike like intrusions, resulting in subvertical isochrons (T1). A rolling-hinge type detachment fault for Atlantis Massif would result in counterclockwise rotation of the crust (T2), juxtaposing younger crust above older. Model 2: Crustal accretion occurs through emplacement of sill-like intrusions (T1), resulting in subhorizontal isochrons. The overall age relationships down core would be relatively unchanged by rotation (T2), except for an increased apparent sill thickness as the borehole is inclined to paleovertical.

the orientation the same section would have when formed at the ridge axis. Multibeam bathymetric mapping of several active detachment fault systems on the MAR near 13°N [*Smith et al.*, 2006, 2008], taken with seismic studies from 26°N MAR [*deMartin et al.*, 2007] suggest that oceanic detachment faults can initiate at high angles, up to 60–70°, and evolve with slip (and attendant rotation) to very gentle dips (<15°). Variably shallow magnetic inclinations in the lower 1.2 km of U1309D (Figure 2) relative to the expected geocentric axial dipole (±49) [*Blackman et al.*, 2006] are consistent with rotations up to ~50° since acquisition of magnetic remanence below 580°C, and support a rolling-hinge model. Significant rotations (up to 90°) have also been interpreted for oceanic core complexes located near the Fifteen-Twenty Fracture Zone along the MAR [*Garcés and Gee*, 2007].

[40] The difference between the dip of the detachment fault on Atlantis Massif where U1309D was drilled (~0°) and the maximum dip of the fault observed adjacent to the eastern block (Figure 1)

implies at least ~12° of counterclockwise rotation of the footwall. As previously mentioned, a much greater degree of rotation is predicted for a fault initiation angle of 60–70° observed on younger oceanic detachment fault systems [*Smith et al.*, 2006; *deMartin et al.*, 2007], and from the magnetic inclination data from Hole U1309D [*Blackman et al.*, 2006].

[41] To determine the effect of rotation on the age progression with depth requires knowledge of the amount of rotation and of the size and shape of the intrusions that construct the crust. If intrusive units are thin (<1.5 km) dikes with vertical sides, rotation would likely produce an apparent younging upward sequence in the core. If, however, the intrusive units are kilometers wide and sill-like with horizontal boundaries, the overall age relationships down core will be relatively unchanged by rotation, except for an increased apparent sill thickness because the borehole would be inclined to paleovertical (Figure 8).

[42] The zircon ages, taken with the petrologic observations, reveal at least two large-scale intrusive series in U1309D (Figure 7), each built by the emplacement of smaller intrusive bodies on the scale of tens of meters. The mean age of the uppermost intrusive series is ~70 ka younger than underlying intrusive series, leading to the suggestion that the section "youngs upward." However, young ages from both Fe-Ti oxide gabbros and felsic dikes are also found in the lower part of the hole (particularly between 1240 and 1330 mbsf), implying the age differences are not simply a consequence of footwall rotation. Further, most models for the construction of lower oceanic crust envision the constructive igneous units to be sill- or pluton-like rather than dike-like [e.g., *Cannat*, 1996; *Korenaga and Kelemen*, 1998]. Likewise, most seismically imaged melt lenses in magmatically active ridge segments are interpreted to have sill-like geometries [e.g., *Dunn et al.*, 2000; *Singh et al.*, 2006]. We therefore do not believe the overall age relationship observed in Hole 1309D is an apparent age relationship created by footwall rotation. Instead, we envisage a crustal section constructed by emplacement of sill-like bodies. The presence of an older intrusion below a younger intrusion implies intrusive activity occurred at different depths below the ridge axis, because sill intrusion at a constant depth in the footwall of a rotating detachment fault would generate a downward younging sequence. Thus, we prefer a model of crustal accretion involving several periods of
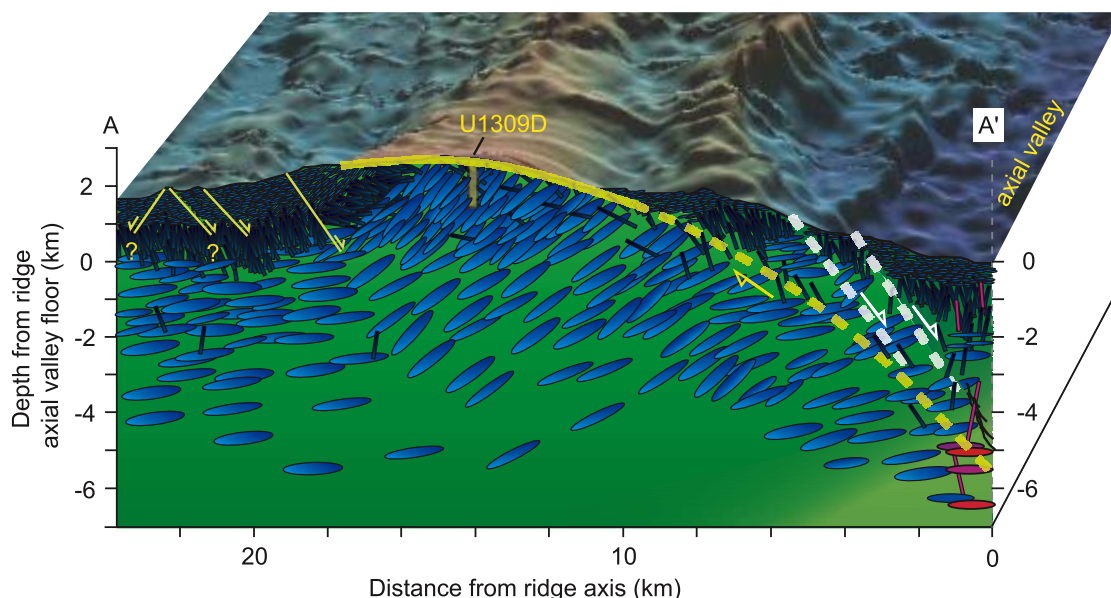
Figure 9. Schematic model for on-axis sill emplacement. True-scale bathymetry (no vertical exaggeration) is shown from cross section A-A′ in Figure 1 across Atlantis Massif. The trace of the detachment fault is shown as a curved, dashed yellow line that becomes more steeply dipping below the rift valley and roots near the zone of active intrusion. The dashed, white lines represent younger normal faults forming the walls of the axial valley. The intrusive crust in the footwall to the detachment fault comprises a series of small-scale sills (shown in blue), which intrude one another to ultimately construct the plutonic lower crust. The red sills and dikes beneath the ridge axis represent active zones of intrusion.
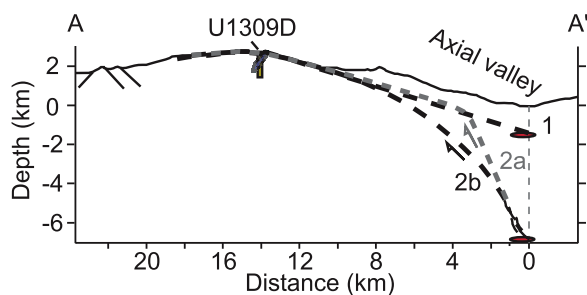
episodic magmatism, focused at different depths in the axial lithosphere (Figure 9). A simple sequence of accretion could involve repeated periods of rapid injection of small, sill-like intrusive bodies to construct a larger intrusive series, followed by a short quiescence before additional magmas are intruded above, below, and into this interval to create the next part of the gabbroic section.

5.3. Spreading Rate at Atlantis Massif

[43] Beyond providing insight into magmatic construction, U-Pb zircon dating can be used to estimate time-integrated detachment fault slip and plate spreading rates. Of primary importance to this discussion is the fact that the gabbro section recovered in U1309D lies in the footwall to a major slip detachment fault exposed on Atlantis Massif; this fault therefore acts as the plate boundary while slip is occurring. To estimate plate-spreading rates it is essential to know the age of the hole, the distance from the present-day ridge axis, the geometry of the fault at depth, and have an estimate of the emplacement/crystallization depth of the recovered gabbro. The emplacement depth of U1309D gabbros is poorly constrained, and we must infer from the literature whether it was

shallow or deep. Geophysical evidence and depths to earthquake epicenters from the nearby TAG segment of the MAR (26°N), where active detachment faulting may be occurring, has been used to suggest magma emplacement at depths below the zone of seismic activity of >5–7 km [*deMartin et al.*, 2007; *Canales et al.*, 2007]. Seismic experiments from other segments of the slow spreading MAR at 37°20′ and 35°N on the MAR, and the intermediate spreading southern Juan de Fuca ridge suggest melt present at depths of ~2.5–3.5 km [e.g., *Singh et al.*, 2006; *Magde et al.*, 2000; *Canales et al.*, 2005]. If we assume crustal accretion occurred "on-axis" at some depth between the limits discussed above, and subsequently moved to the surface along a curved fault, we can calculate the distance crust recovered in U1309D has traveled since formation ~1.2 million years ago, and evaluate associated spreading rates.

[44] Estimates for the transport distance of gabbro emplaced beneath the ridge axis at 2 and 7 km depth are shown in Figure 10. The models use the true bathymetry across Atlantis Massif from cross section A-A′ (Figure 1). Both a continuously curved fault and a two-segment fault with a tight radius of curvature (similar to the fault geometry

Depth of Emplacement	Transport Distance	Transport Rate
Path 1: 2 km	14.6 km	12.2 km/my
Path 2a: 7 km (two segment)	18.8 km	15.7 km/my
Path 2b: 7 km (constant curvature)	18.1 km	15.0 km/my

Figure 10. Model transport paths for gabbros in U1309D from emplacement beneath the ridge axis to the current position off-axis. We show two extremes for gabbro crystallization: Path 1. Gabbro crystallizes near the seafloor just below the axial valley. This model gives a slip/spreading rate ≈ half spreading rate and does not predict footwall rotation. Path 2. Gabbro crystallizes at 7 km depth. Two fault geometries are shown: constant curvature and a two-segment fault. The two-segment fault has a tight radius of curvature, similar to the fault geometry inferred by *deMartin et al.* [2007]. The constant curvature fault trace is drawn to match the curvature on the central dome of Atlantis Massif. These models indicate a time-averaged spreading rate of 12.2– 15.7 mm/a, equating to as much as ~70% asymmetry in plate spreading, and imply substantial rotation of the footwall. Note: these depths are indicative of the last stages of crystallization (i.e., timing of zircon saturation) and may not reflect depths for the onset of gabbro crystallization.

inferred by *deMartin et al.* [2007]) are used. The resulting range of transport distances is 14.6 to 18.8 km, equating to mean spreading rates for the last 1.2 Ma of 12.2–15.7 mm/a (using the mean age of 1.20 Ma from all samples dated in U1309D). The minimum rate observed equates to gabbro emplaced at 2 km below the seafloor, and is similar to the regional half spreading rate of ~12 mm/a [e.g., *Zervas et al.*, 1995]. Faster rates corresponding to ~70% of the full plate-spreading rate during formation of Atlantis Massif are consistent with emplacement at depths of 7 km below the ridge axis, and imply asymmetric plate spreading during detachment faulting. Emplacement at greater depths would of course predict even faster spreading. The models with deeper gabbro em-

placement involving uplift along a rolling-hinge type detachment fault are preferred since they also predict footwall rotation consistent with the magnetic inclination data (Figure 9).

[45] Determining the spreading rate from a single point (U1309D) and an estimated transport distance provides only the time-averaged spreading rate over the last 1.2 Ma. Evaluating additional samples from the southern ridge located across Atlantis Massif with different distances from the ridge axis affords an estimate of spreading rate and fault slip rate not requiring an estimate of gabbro emplacement depth. An error-weighted regression through 5 of these samples (excluding 3652–1333, because it is anomalously old) and U1309D yields a rate of 28.7 ± 6.7 mm/a (error at 95% confidence) (Figure 11). Excluding the poorly constrained dredge sample, D3-21, a statistically indistinguishable rate of 26.5 ± 6.2 mm/a can be determined. Overall, this rate is slightly faster than, but within error of, the full spreading rate at 30°N, MAR (~23.6 mm/a), and implies 100% asymmetric accretion on the North American plate for at least 0.2 million years (the age range of the samples). We believe that this is a true spreading rate and not an erroneous rate created by samples being out of place having been left behind on the footwall as debris or fault slivers from the hanging wall. This locally fast rate is consistent with a time averaged spreading rate of ~16 mm/a over the last 1.2 Ma determined assuming crystallization of the U1309D gabbros at depths of 7 km, but requires spreading at the full plate spreading rate during the formation of Atlantis Massif followed by a slower plate spreading rate of 12 mm/a over the last 1 Ma following cessation of detachment fault slip (Figure 11b).

[46] One sample from the southern ridge, 3652–1333, falls significantly above the trend defined by the remaining samples in the study area owing to the fact that it is 0.5–0.6 Ma older than nearby sample 3652–1002. An anomalously old age could be generated if a block from the hanging wall breaks off and is attached to the footwall long after it crystallized. However, in this case the age discrepancy of 0.5–0.6 Ma together with a spreading rate of 16 mm/a requires the block to be ~8–10 km out of place. This "restored distance" lies several kilometers beyond (west) the proposed breakaway to the detachment fault system [*Blackman et al.*, 2006], making it unlikely that this sample is debris clipped off the hanging wall. A more plausible explanation for this age discrepancy is that the
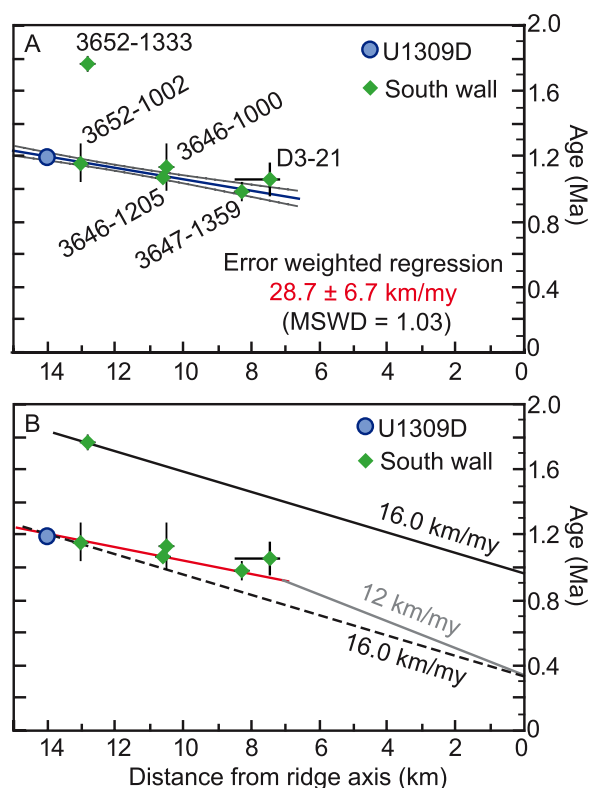
Figure 11. Age versus distance plots for samples dated across the southern wall of Atlantis Massif and U1309D. Off-axis distances have been determined by projecting samples onto cross-section line A-A′ (Figure 1) and measuring to the midpoint of the current magnetic normal polarity event [from *Pariso et al.*, 1996]. The slope of the seafloor was taken into account when determining distance. (a) Error-weighted regression through samples from the southern ridge of Atlantis Massif (excluding 3652–1333) and Hole U1309D with error envelope. (b) Model for short-lived spreading at the full plate separation rate of 24 mm/a, as indicated in Figure 11a, between 1.2 and 0.95 Ma followed by spreading at the regional half-rate of 12 mm/a over the past 0.95 Ma. This model is consistent with a time-averaged spreading rate of ∼16 mm/a since the crystallization of U1309D gabbros.

rcon from this sample crystallized at greater depths than the majority of the crust. For this scenario to be consistent with the time-averaged spreading rate of ∼16 mm/a, 3652–1333 would have had to have been emplaced ∼10 km deeper than the evolved samples dated in U1309D, or depths of 16–17 km (based on Figure 11). An interpretation involving variable emplacement depths is consistent with the suggestion by *Schwartz et al.* [2005] that anomalously old sample ages at Atlantis Bank (25% of all samples dated from the surface) suggest crystallization as deep as 18 km, followed by uplift and

entrainment by shallower magmatism that constructed most of the crust. The presence of a single anomalously old sample in our sample set precludes any conclusive interpretation, but deep emplacement seems the most plausible explanation.

[47] Asymmetric spreading has been hypothesized as a significant aspect of plate separation at slow spreading ridge settings [e.g., *Karson*, 1990; *Lagabrielle et al.*, 1998; *Allerton et al.*, 2000; *Baines et al.*, 2007]. In recent years, asymmetric spreading has been reported over two core complexes located along the Southwest Indian Ridge (SWIR). At Atlantis Bank (57°E SWIR), both magnetic and U-Pb zircon dating reveal highly asymmetric magmatic accretion (up to 80%) during formation [*Baines et al.*, 2008]. Over Fuji Dome (63°45′ SWIR), spreading rates of ∼77% of the full rate are inferred from magnetic anomaly data [*Searle et al.*, 2003]. Additionally, seafloor spreading has been interpreted to have been highly asymmetric during formation of the Kane core complexes at 23°N on the MAR on the basis of magnetic anomalies [*Williams*, 2007]. These are consistent with the data from Atlantis Massif, which indicate spreading at 70–100% of the full plate separation rate. The interpretation of more rapid spreading than the average plate spreading half-rate across numerous core complexes located along multiple ridge systems suggests that slip on detachment faults, asymmetric spreading, and associated ridge migration play an integral role in the formation of oceanic core complexes.

6. Conclusions

[48] Zircon crystallization ages obtained from over a 1.4 km vertical borehole (IODP Hole U1309D) span 200 (±120) ka, indicating protracted magma emplacement for this section of slow spread crust. This time period is a minimum duration estimate for the magmatic construction of gabbroic crust sampled by U1309D, as dated rocks are intrusive into less evolved gabbro and olivine gabbro; younger diabase cut the entire section. The duration of magmatism is similar to the >210,000 years of magma emplacement reported for gabbros from the MARK area [*Meurer and Gee*, 2002].

[49] Two distinct ages are recognized in U1309D, though they are distributed such as to indicate potentially three separate intrusive events. The older age of 1.24 ± 0.02 Ma corresponds to lithologic supergroup II and the deepest sample

studied, D1415. The younger age of 1.17 ± 0.02 Ma corresponds to lithologic supergroup I, and is consistent with other samples distributed throughout the hole. These data suggest episodic periods of intrusive activity on a timescale of $\sim$70 ka. On the basis of core observations of over 250 intrusive contacts and the possible duration of accretion recorded by Pb/U zircon ages, the lithologic supergroups in U1309D could have been formed by on average one 10 m thick injection of magma on the order of every $\sim$1000 years. The presence of younger rocks above older rocks into which younger rocks are intruded requires variable depths of intrusion beneath the axial valley.

[50] The time-averaged spreading rate for the last 1.2 Ma over Atlantis Massif appears to have been $\sim$70% of the full plate-spreading rate, on the basis of an estimated emplacement depth of 7 km for Hole U1309D gabbros. The ages of samples distributed across the surface of Atlantis Massif along with the age of U1309D imply 100% asymmetric spreading for at least 200 ka during the formation of this core complex.

[51] One anomalously old sample (by $\sim$0.5 Ma) was collected from the southern ridge (3652–1333). We suggest this sample may have crystallized at anomalous depths up to 10 km greater than other samples in this study, or $\sim$17 km below the axial valley, followed by continued magmatism, upwelling, and denudation to the seafloor.

Acknowledgments

References

Aldiss, D. T. (1981), Plagiogranites from the ocean crust and ophiolites, *Nature*, *289*, 577–578, doi:10.1038/289577a0.

Allerton, S., J. Escartín, and R. C. Searle (2000), Extremely asymmetric magmatic accretion of oceanic crust at the ends of slow-spreading ridge segments, *Geology*, *28*, 179–182, doi:10.1130/0091-7613(2000)28<179:EAMAOO>2.0.CO;2.

Baines, A. G. (2006), Geodynamic investigation of ultra-slow spreading oceanic lithosphere; Atlantis Bank and vicinity, SW Indian Ridge, Ph.D. dissertation, 212 pp., Univ. of Wyoming, Laramie.

Baines, A. G., M. J. Cheadle, H. J. B. Dick, A. Hosford Scheirer, B. E. John, N. J. Kusznir, and T. Matsumoto (2007), The evolution of the Southwest Indian Ridge from 55°45′E to 62°E: Changes in plate-boundary geometry since 26 Ma, *Geochem. Geophys. Geosyst.*, *8*, Q06022, doi:10.1029/2006GC001559.

Baines, A. G., M. J. Cheadle, B. B. John, and J. J. Schwartz (2008), The rate of oceanic detachment faulting at Atlantis Bank, SW Indian Ridge, *Earth Planet. Sci. Lett.*, doi:10.1016/j.epsl.2008.06.013, in press.

Blackman, D. K., J. R. Cann, B. Janssen, and D. K. Smith (1998), Origin of extensional core complexes: Evidence from the Mid-Atlantic Ridge at Atlantis Fracture Zone, *J. Geophys. Res.*, *103*, 21,315–21,333, doi:10.1029/98JB01756.

Blackman, D. K., et al. (2002), Geology of the Atlantis Massif (Mid-Atlantic Ridge, 30°N): Implications for the evolution of an ultramafic oceanic core complex, *Mar. Geophys. Res.*, *23*, 443–469, doi:10.1023/B:MARI.0000018232.14085.75.

Blackman, D. K., B. Ildefonse, B. E. John, Y. Ohara, D. J. Miller, C. J. MacLeod, and Expedition 304/305 Scientists (2006), *Proceedings of the Integrated Ocean Drilling Program*, vol. 304/305, Integrated Ocean Drill. Program Manage. Int. Inc., College Station, Tex., doi:10.2204/iodp.proc.304305.2006.

Boschi, C., G. L. Früh-Green, A. Delacour, J. A. Karson, and D. S. Kelley (2006), Mass transfer and fluid flow during detachment faulting and development of an oceanic core complex, Atlantis Massif (MAR 30°N), *Geochem. Geophys. Geosyst.*, *7*, Q01004, doi:10.1029/2005GC001074.

Botcharnikov, R. E., J. Koepke, and F. Holtz (2008), Experimental phase relations, mineral-melt equilibria and liquid lines of descent in a hydrous ferrobasalt—Implications for the Skaargaard Intrusion and other natural systems *J. Petrol.*, in press.

Buck, W. R. (1988), Flexural rotation of normal faults, *Tectonics*, *7*, 959–973, doi:10.1029/TC007i005p00959.

Buck, W. R., L. L. Lavier, and A. N. B. Poliakov (2005), Modes of faulting at mid-ocean ridges, *Nature*, *434*, 719–723, doi:10.1038/nature03358.

Canales, J. P., R. S. Detrick, S. M. Carbotte, G. M. Kent, J. B. Diebold, A. Harding, J. Babcock, M. R. Nedimović, and E. van Ark (2005), Upper crustal structure and axial topography at intermediate spreading ridges: Seismic constraints from the southern Juan de Fuca Ridge, *J. Geophys. Res.*, *110*, B12104, doi:10.1029/2005JB003630.

Canales, J. P., R. A. Sohn, and B. J. deMartin (2007), Crustal structure of the Trans-Atlantic Geotraverse (TAG) segment (Mid-Atlantic Ridge, 26°10′N): Implications for the nature of hydrothermal circulation and detachment faulting at slow spreading ridges, *Geochem. Geophys. Geosyst.*, *8*, Q08004, doi:10.1029/2007GC001629.

Cande, S. C., and D. V. Kent (1995), Revised calibration of the geomagnetic polarity timescale for the Late Cretaceous and Cenozoic, *J. Geophys. Res.*, *100*, 6093–6095, doi:10.1029/94JB03098.

Cann, J. R., D. K. Blackman, D. K. Smith, E. Mcallister, B. Janssen, S. Mello, E. Avgerinos, A. R. Pascoe, and J. Escartin (1997), Corrugated slip surfaces formed at ridge-transform intersections on the Mid-Atlantic Ridge, *Nature*, *385*, 329–332, doi:10.1038/385329a0.

Cannat, M. (1996), How thick is the magmatic crust at slow spreading oceanic ridges?, *J. Geophys. Res.*, *101*, 2847–2857, doi:10.1029/95JB03116.

Cannat, M., and J. F. Casey (1995), An ultramafic lift at the Mid-Atlantic Ridge: Successive stages of magmatism in serpentinized peridotite from the 15°N region, in *Mantle and Lower Crust Exposed in Oceanic Ridges and in Ophiolites*, edited by R. L. M. Vissers and A. Nicolas, pp. 5–34, Kluwer Acad., Norwell, Mass.

Claiborne, L. L., C. F. Miller, B. A. Walker, J. L. Wooden, F. K. Mazdab, and F. Bea (2006), Tracking magmatic processes through Zr/Hf ratios in rocks and Hf and Ti zoning in zircons: An example from the Spirit Mountain batholith, Nevada, *Mineral. Mag.*, *70*, 517–543, doi:10.1180/0026461067050348.

Coleman, R. G., and M. M. Donato (1979), Oceanic plagiogranite revisited, in *Trondjhemites, Dacites, and Related Rocks*, pp. 149–167, Elsevier, Amsterdam.

Coogan, L. A., and R. W. Hinton (2006), Do the trace element compositions of detrital zircons require Hadean continental crust?, *Geology*, *34*, 633–636, doi:10.1130/G22737.1.

Coogan, L. A., R. N. Wilson, K. M. Gillis, and C. J. MacLeod (2001), Near-solidus evolution of oceanic gabbros: Insights from amphibole geochemistry, *Geochim. Cosmochim. Acta*, *65*, 4339–4357, doi:10.1016/S0016-7037(01)00714-1.

Coogan, L. A., G. R. T. Jenkin, and R. N. Wilson (2002), Constraining the cooling rate of the lower oceanic crust: A new approach applied to the Oman Ophiolite, *Earth Planet. Sci. Lett.*, *199*, 127–146, doi:10.1016/S0012-821X(02)00554-X.

Corfu, F., J. M. Hanchar, P. W. O. Hoskin, and P. Kinney (2003), Atlas of zircon textures, in *Zircon*, *Rev. Mineral. Geochem.*, vol. 53, edited by J. M. Hanchar and P. W. O. Hoskin, pp. 469–500, Mineral. Soc. of Am., Washington, D. C.

Davis, G. A., and G. S. Lister (1988), Detachment faulting in continental extension: Perspectives from the southwestern U.S. Cordillera, in *Processes in Continental Lithospheric Deformation*, edited by S. P. Clark et al., *Spec. Pap. Geol. Soc. Am.*, *218*, 133–159.

deMartin, B. J., R. A. Sohn, J. P. Canales, and S. E. Humphris (2007), Kinematics and geometry of active detachment faulting beneath the Trans-Atlantic Geotraverse (TAG) hydrothermal field on the Mid-Atlantic Ridge, *Geology*, *35*, 711–714, doi:10.1130/G23718A.1.

Dick, H. J. B., et al. (2000), A long in situ section of lower ocean crust: Results of ODP Leg 176 drilling at the Southwest Indian Ridge, *Earth Planet. Sci. Lett.*, *179*, 31–51, doi:10.1016/S0012-821X(00)00102-3.

Dunn, R. A., D. R. Toomey, and S. C. Solomon (2000), Three-dimensional seismic structure and physical properties of the crust and shallow mantle beneath the East Pacific Rise at 9°30′N, *J. Geophys. Res.*, *105*(B10), 23,537–23,555, doi:10.1029/2000JB900210.

Ferry, J. M., and E. B. Watson (2007), New thermodynamic models and revised calibrations for the Ti-in-zircon and Zr-in-rutile thermometers, *Contrib. Mineral. Petrol.*, *154*, 429–437, doi:10.1007/s00410-007-0201-0.

Garcés, M., and J. S. Gee (2007), Paleomagnetic evidence of large footwall rotations associated with low-angle faults at the Mid-Atlantic Ridge, *Geology*, *35*, 279–282, doi:10.1130/G23165A.1.

Gee, J., and D. Blackman (2004), Lineated near bottom magnetic anomalies over an oceanic core complex, Atlantis Massif (Mid-Atlantic Ridge at 30°N), *Eos Trans. AGU*, *85*(17), Jt. Assem. Suppl., Abstract GP31A-15.

Geisler, T., U. Schaltegger, and F. Tomaschek (2007), Re-equilibration of zircon in aqueous fluids and melts, *Elements*, *3*, 43–50, doi:10.2113/gselements.3.1.43.

Gillis, K., et al. (1993), *Proceedings of the Ocean Drilling Program, Initial Reports*, vol. 147, Ocean Drill. Program, College Station, Tex., doi:10.2973/odp.proc.ir.147.1993.

Grimes, C. B., B. E. John, and J. L. Wooden (2007a), Protracted construction of gabbroic crust at a slow-spreading ridge: Constraints from SHRIMP Pb/U zircon ages in IODP hole 1309D, Atlantis Massif, MAR (30°N), *Eos Trans. AGU*, *88*(52), Fall Meet. Suppl., Abstract T52B-03.

Grimes, C. B., B. E. John, P. B. Kelemen, F. Mazdab, J. L. Wooden, M. J. Cheadle, K. Hanghøj, and J. J. Schwartz (2007b), The trace element chemistry of zircons from oceanic crust: A method for distinguishing detrital zircon provenance, *Geology*, *35*, 643–646, doi:10.1130/G23603A.1.

Hanchar, J. M., and C. F. Miller (1993), Zircon zonation patterns as revealed by cathodoluminscence and backscattered electron images: Implications for interpretation of complex crustal histories, *Chem. Geol.*, *110*, 1–13, doi:10.1016/0009-2541(93)90244-D.

Hoskin, P. W. O., and U. Schaltegger (2003), The composition of zircon and igneous and metamorphic petrogenesis, in *Zircon*, *Rev. Mineral. Geochem.*, vol. 53, edited by J. M. Hanchar and P. W. O. Hoskin, pp. 27–62, Mineral. Soc. of Am., Washington, D. C.

Ildefonse, B., D. K. Blackman, B. E. John, D. J. Miller, C. J. MacLeod, and Expedition 304/305 Shipboard Science Party (2007), Oceanic core complexes and crustal accretion at slow-spreading ridges, *Geology*, *35*, 623–626, doi:10.1130/G23531A.1.

Ireland, T. R., and I. S. Williams (2003), Considerations in zircon geochronology by SIMS, in *Zircon*, *Rev. Mineral. Geochem.*, vol. 53, edited by J. M. Hanchar and P. W. O. Hoskin, pp. 215–241, Mineral. Soc. of Am., Washington, D. C.

John, B. (1987), Geometry and evolution of a mid-crustal extension fault system: Chemeuevi Mountains, southeastern California, in *Continental Extensional Tectonics*, edited by M. P. Coward, J. F. Dewey, and P. L. Hancock, *Geol. Soc. Spec. Publ.*, *28*, 313–335.

John, B. E., D. A. Foster, J. M. Murphy, M. J. Cheadle, A. G. Baines, M. Fanning, and P. Copeland (2004), Determining the cooling history of in situ lower oceanic crust—Atlantis bank, SW Indian Ridge, *Earth Planet. Sci. Lett.*, *222*, 145–160, doi:10.1016/j.epsl.2004.02.014.

John, B. E., D. Blackman, B. Ildefonse, Y. Ohara, and J. Miller (2006), Crustal accretion and denudation processes at slow spreading MOR—Insight from IODP Hole U1309D (MAR 30°N), *Eos Trans. AGU*, *86*(52), Fall Meet. Suppl., Abstract T33G-04.

Johnson, K. T., et al. (2005), Igneous petrology of Hole U1309D, IODP Expeditions 304/305 at the Atlantis Massif, MAR 30°N, *Eos Trans. AGU*, *86*(52), Fall Meet. Suppl., Abstract T41D-1336.

Karson, J. A. (1990), Seafloor spreading on the Mid-Atlantic Ridge: Implications for the structure of ophiolites and oceanic lithosphere produced in slow-spreading environments, in *Ophiolites and Oceanic Crustal Analogues: Proceedings of the Symposium "Troodos 1987"*, edited by J. Malpas et al., pp. 125–130, Geol. Surv. Dep., Nicosia, Cyprus.

Karson, J. A., G. L. Früh-Green, D. S. Kelley, E. A. Williams, D. R. Yoerger, and M. Jakuba (2006), Detachment shear zone of the Atlantis Massif core complex, Mid-Atlantic Ridge, 30°N, *Geochem. Geophys. Geosyst.*, *7*, Q06016, doi:10.1029/2005GC001109.

Kelemen, P. B., et al. (2004), *Proceedings of the Ocean Drilling Program, Initial Reports*, vol. 209, Ocean Drill. Program, College Station, Tex., doi:10.2973/odp.proc.ir.209.2004.

Koepke, J., S. T. Feig, J. Snow, and M. Friese (2004), Petrogenesis of oceanic plagiogranites by partial melting of gabbros: An experimental study, *Contrib. Mineral. Petrol.*, *146*, 414–432, doi:10.1007/s00410-003-0511-9.

Koepke, J., J. Berndt, S. T. Feig, and F. Holtz (2007), The formation of SiO_2-rich melts within deep oceanic crust by hydrous partial melting of gabbros, *Contrib. Mineral. Petrol.*, *153*, 67–84, doi:10.1007/s00410-006-0135-y.

Korenaga, J., and P. B. Kelemen (1998), Melt migration through the oceanic lower crust: A constraint from melt percolation modeling with finite solid diffusion, *Earth Planet. Sci. Lett.*, *156*, 1–11, doi:10.1016/S0012-821X(98)00004-1.

Lagabrielle, Y., D. Bideau, M. Cannat, J. A. Karson, and C. Mevel (1998), Ultramafic-mafic plutonic rock suites exposed along the Mid-Atlantic Ridge (10°N–30°N): Symmetrical-asymmetrical distribution and implications for seafloor spreading processes, in *Faulting and Magmatism at Mid-ocean Ridges*, *Geophys. Monogr. Ser*, vol. 106, edited by W. R. Buck, pp. 153–176, AGU, Washington, D. C.

Lavier, L. L., W. R. Buck, and A. N. B. Poliakov (1999), Self-consistent rolling-hinge model for the evolution of large-offset low-angle normal faults, *Geology*, *27*, 1127–1130, doi:10.1130/0091-7613(1999)027<1127:SCRHMF>2.3.CO;2.

Ludwig, K. R. (2001), SQUID: A user's manual, *Berkeley Geochronol. Cent. Spec. Publ., 2*, 22 pp., Berkeley, Calif.

Ludwig, K. R. (2003), User's manual for isoplot 3.00: A geochronological toolkit for Microsoft Excel, *Berkeley Geochronol. Cent. Spec. Publ.*, *4*, 71 pp., Berkeley, Calif.

Maclennan, J., T. Hulme, and S. C. Singh (2005), Cooling of the lower oceanic crust, *Geology*, *33*, 357–360, doi:10.1130/G21207.1.

Magde, L. S., A. H. Barclay, D. R. Toomey, R. S. Detrick, and J. A. Collins (2000), Crustal magma plumbing within a segment of the Mid-Atlantic Ridge, 35°N, *Earth Planet. Sci. Lett.*, *175*, 55–67, doi:10.1016/S0012-821X(99)00281-2.

Mazdab, F. K., and J. L. Wooden (2006), Trace element analysis in zircon by ion microprobe (SHRIMP-RG): Technique and applications, *Geochim. Cosmochim. Acta*, *70*, A405, doi:10.1016/j.gca.2006.06.817.

Meurer, W. P., and J. Gee (2002), Evidence for the protracted construction of slow-spread oceanic crust by small magmatic injections, *Earth Planet. Sci. Lett.*, *201*, 45–55, doi:10.1016/S0012-821X(02)00660-X.

Natland, J. H., and H. J. B. Dick (2002), Stratigraphy and composition of gabbros drilled in Ocean Drilling Program Hole 735B, Southwest Indian Ridge: A synthesis of geochemical data, *Proc. Ocean Drill. Program Sci. Results*, *176*, 1–69.

Natland, J. H., P. S. Meyer, H. J. B. Dick, and S. H. Bloomer (1991), Magmatic oxides and sulfides in gabbroic rocks from Hole 735B and the later development of the liquid line of descent, *Proc. Ocean Drill. Program Sci. Results*, *118*, 75–111, doi:10.2973/odp.proc.sr.118.163.1991.

Niu, Y., T. Gilmore, S. Mackie, A. Greig, and W. Bach (2002), Mineral chemistry, whole-rock compositions, and petrogenesis of Leg 176 gabbros: Data and discussion, *Proc. Ocean Drill. Program Sci. Results, 176*, 60 pp. (Available at http://www.odp.tamu.edu.publications/176_SR/ VOLUME/CHAPTERS/SR176_08.PDF)

Pariso, J. E., C. Rommevaux, and J.-C. Sempere (1996), Three-dimensional inversion of marine magnetic anomalies: Implications for crustal accretion along the Mid-Atlantic Ridge (28°–31°30′N), *Mar. Geophys. Res.*, *18*, 85–101, doi:10.1007/BF00286204.

Parrish, R. R., and N. R. Noble (2003), Zircon U-Th-Pb geochronology by isotope dilution—Thermal ionization mass spectrometry (ID-TIMS), in *Zircon*, *Rev. Mineral. Geochem.*, vol. 53, edited by J. M. Hanchar and P. W. O. Hoskin, pp. 182–213, Mineral. Soc. of Am., Washington, D. C.

Robinson, P. T., J. Erzinger, and R. Emmermann (2002), The composition and origin of igneous and hyrothermal veins in the lower ocean crust—ODP Hole 735B, Southwest Indian Ridge, *Proc. Ocean Drill. Program Sci. Results, 176*, 66 pp., doi:10.2973/odp.proc.sr.176.019.2002.

Schroeder, T., and B. E. John (2004), Strain localization on an oceanic detachment fault system, Atlantis Massif, 30°N, Mid-Atlantic Ridge, *Geochem. Geophys. Geosyst.*, *5*, Q11007, doi:10.1029/2004GC000728.

Schwartz, J., B. E. John, M. J. Cheadle, E. Miranda, C. B. Grimes, J. Wooden, and H. J. B. Dick (2005), Inherited zircon and the magmatic construction of oceanic crust, *Science*, *310*, 654–657, doi:10.1126/science.1116349.

Scoates, J. S., and K. R. Chamberlain (1995), Baddelyite (ZrO_2) and zircon ($ZrSiO_4$) from anorthositic rocks of the Laramie anorthosite complex, Wyoming: Petrologic consequences and U-Pb age, *Am. Mineral.*, *80*, 1317–1327.

Searle, R. C., M. Cannat, K. Fujioka, C. Mével, H. Fujimoto, A. Bralee, and L. Parson (2003), FUJI Dome: A large detachment fault near 64°E on the very slow-spreading southwest Indian Ridge, *Geochem. Geophys. Geosyst.*, *4*(8), 9105, doi:10.1029/2003GC000519.

Singh, S. C., W. C. Crawford, H. Carton, T. Seher, V. Combier, M. Cannat, J. P. Canales, D. Düsünür, J. Escartin, and J. M. Miranda (2006), Discovery of a magma chamber and faults beneath a Mid-Atlantic Ridge hydrothermal field, *Nature*, *442*, 1029–1032, doi:10.1038/nature05105.

Smith, D. K., J. R. Cann, and J. Escartin (2006), Widespread active detachment faulting and core complex formation near 13°N on the Mid-Atlantic Ridge, *Nature*, *442*, 440–443, doi:10.1038/nature04950.

Smith, D. K., J. Escartín, H. Schouten, and J. R. Cann (2008), Fault rotation and core complex formation: Significant processes in seafloor formation at slow-spreading mid-ocean ridges (Mid-Atlantic Ridge, 13°–15°N), *Geochem. Geophys. Geosyst.*, *9*, Q03003, doi:10.1029/2007GC001699.

Stacey, J. S., and J. D. Kramers (1975), Approximation of terrestrial lead isotope evolution by a two-stage model, *Earth Planet. Sci. Lett.*, *26*, 207–221, doi:10.1016/0012-821X(75)90088-6.

Tera, F., and G. J. Wasserburg (1972), U-Th-Pb systematics in three Apollo 14 basalts and the problem of initial Pb in lunar rocks, *Earth Planet. Sci. Lett.*, *14*, 281–304, doi:10.1016/0012-821X(72)90128-8.

Tucholke, B. E., and J. Lin (1994), A geological model for the structure of ridge segments in slow spreading ocean crust, *J. Geophys. Res.*, *99*, 11,937–11,958, doi:10.1029/94JB00338.

Watson, E. B., D. A. Wark, and J. B. Thomas (2006), Crystallization thermometers for zircon and rutile, *Contrib. Mineral. Petrol.*, *151*, 413–433, doi:10.1007/s00410-006-0068-5.

Wessel, P., and W. H. F. Smith (1998), New improved version of Generic Mapping Tools released, *Eos Trans. AGU*, *79*(47), 579, doi:10.1029/98EO00426.

Williams, C. M. (2007), Oceanic lithosphere magnetization: Marine magnetic investigations of crustal accretion and tec-

tonic processes in mid-ocean ridge environments, Ph.D. dissertation, Mass. Inst. of Technol., Woods Hole Oceanogr. Inst., Cambridge, Mass.

Williams, I. S., and J. M. Hergt (2000), U-Pb dating of Tasmanian dolerites: A cautionary tale of SHRIMP analysis of high-U zircon., in *Beyond 2000: New Frontiers in Isotope Geoscience, Lorne, 2000*, edited by J. D. Woodhead, J. M.

Hergt, and W. P. Noble, pp. 185–188, Univ. of Melbourne, Melbourne, Australia.

Zervas, C. E., J.-C. Sempere, and J. Lin (1995), Morphology and crustal structure of a small transform fault along the Mid-Atlantic Ridge: The Atlantis Fracture Zone, *Mar. Geophys. Res.*, 17, 275–300, doi:10.1007/BF01203466.